PHYSICS IV 2012

Critical Quantum Lattice Models using the Multiscale Entanglement Renormalisation Ansatz

Jacob Bridgeman
Centre for Engineered Quantum Systems
School of Physics
The University of Sydney

Abstract

The simulation of quantum systems on classical computers is typically hard. We have developed an algorithm to efficiently optimise the multiscale entanglement renormalisation ansatz to represent the ground state of a large class of critical quantum spin chains. By incorporating Abelian symmetries, we achieve a multiplicative reduction in the computational resources required to implement the algorithm. Further, we have incorporated an approximation into the algorithm, allowing for an improvement in the scaling of the algorithm with χ, the parameter controlling the accuracy of the approximation to the ground state. We have demonstrated the reduced computational requirements of these modified algorithms.

Using the MERA, we examine a pair of models with complex phase diagrams; the Ashkin-Teller and perturbed cluster spin chains. We show how data corresponding to a quantum field theory can be extracted from simulating these lattices, and demonstrate the ability to recover the behaviour of the model as the scale invariant ground state is varied.

Acknowledgements

I would like to thank my supervisors Stephen Bartlett and Andrew Doherty for all their help and support over the last two years. Thanks also go to Aroon O'Brien. I would also like to thank Guifre Vidal for informative discussions at the 2012 Sydney Quantum Information Theory Workshop, which led to many of the innovations used in this project. Many thanks to Andrew Darmawan for questions and comments leading to clarifications in my explanation of various concepts. Lastly I would like to thank everyone for their patience and understanding concerning my substantial and prolonged computational requirements. Particular thanks to the experimental students and staff for sacrificing computer time.

Statement of Student Contribution

This project was a theoretical investigation into spin lattices and the field theories describing them. This took the form of a numerical examination of two models using a new method known as the multiscale entanglement renormalisation ansatz (MERA). This required developing code to implement an existing algorithm, and developing new modifications to improve the efficiency and accuracy. All the code required to implement the algorithm was developed and written by myself. All analysis and interpretation of the results are my own work. Chapters 1 and 2 contain review material. The remaining sections reflect my own contributions.

The MERA was first proposed in 2007 by Guifre Vidal [1]. Later, an algorithm was developed to optimise the network [2–5]. This algorithm is reviewed in chapter 2 of this thesis. All the code required to implement the algorithm was developed by myself.

The various innovations incorporated into my MERA implementation are documented in chapter 3. The development and writing of code to incorporate these was entirely my own work. Following discussions at the 2012 Sydney Quantum Information Theory Workshop, Stephen, Andrew and myself decided to implement a MERA which incorporated the symmetries present in the models of interest. This allows for a more computationally efficient code. The modifications made were implemented entirely by me using ideas from [6–8].

The preprocessing algorithm described in chapter 3 was developed entirely by myself, following the discussions at the workshop.

The idea to include a projector into the ternary MERA was entirely my own. This was based on a description in [4], however to the best of my knowledge this has not been incorporated into the ternary MERA previously, thus the specific implementation and tuning required was entirely my own work. This is described in chapter 3. The projector is particularly important, as it gives a major improvement to the scaling of the algorithm, and brings much more accurate MERA within computational reach.

My supervisors proposed investigating the connection between the Ashkin-Teller and cluster models, based on a link first noted in [9]. Using a generalisation of a map described in [9], I constructed the perturbed cluster model. The mappings used to construct this model and formalise the equivalence is presented in appendix D. The idea to use the MERA to investigate this model directly was my own. This led to an identification with the XXZ model, allowing me to conjecture the conformal field theory describing the thermodynamic limit of the perturbed cluster model.

I certify that this report contains work carried out

by myself except where otherwise acknowledged.

Jacob Bridgeman

Tuesday 27th November, 2012

Contents

Chapter 1

Introduction

The study of interacting quantum systems lies at the heart of much of modern science, including condensed matter, atomic and particle physics, computational chemistry and quantitative biology. A wide variety of techniques have been developed to analyse these many body systems. Weakly interacting systems can be attacked using perturbative techniques, but some of the most interesting systems are those which are strongly interacting. In particular, many condensed matter systems contain very strong interactions, and very few methods exist which can be applied to general models. In the field of quantum computation there has been much interest in highly entangled ground states, which can be used for quantum computation requiring only measurement [10].

Recently, a new class of methods has been described which allow much more general investigation of strongly interacting quantum systems. Known as tensor network algorithms, these use a complex network of tensors to efficiently approximate the true ground state of interacting systems, and allow the determination of correlations, expectation values and energies. In this thesis, we will describe a particularly powerful tensor network know as the multiscale entanglement renormalisation ansatz (MERA). This was first proposed in 2007 by Guifre Vidal [1], with an optimisation algorithm following in 2009 [2]. This network allows for the analysis of the most entangled many body systems in one dimension, the *critical* models. These models are characterised by their infinite correlation length, and are among the most resistant models to numerical simulation.

In this thesis, we apply the MERA to a new class of models, which have been little studied using these methods. In particular, we wish to analyse the quantum Ashkin-Teller model, an antiferromagnetic spin chain which has been under investigation for over 30 years, and the perturbed cluster Hamiltonian, related to a resource state for quantum computation. We develop modifications to the basic MERA algorithm, making it more computationally efficient. The MERA is then used to investigate the properties of a class of models far more complex than those previously investigated.

In chapter one, some formalism and physical concepts required for this thesis are reviewed. In particular, we describe the type of models we will analyse, the one dimensional critical lattice models. We also discuss conformal field theories; quantum field theories which describe the thermodynamic properties of these lattice models, and who's properties constitute the bulk of the physical information which we will extract from the MERA.

In chapter two, we will review an algorithm which can be used to numerically optimise the MERA to accurately approximate the ground states of this highly entangled systems. By implementing this algorithm, we can simulate the lattice model and furthermore, we can extract information pertaining to the conformal field theory describing the thermodynamic limit of the spin chain. We explain how this data can be extracted.

From chapter three onwards, we present original work. We begin by introducing our modifications, which both improve the description and reduce the resources required for the algorithm. By reducing the time required by the algorithm, we are able to obtain results which go beyond the literature.

In chapter four, we will describe two models, the Ashkin-Teller and perturbed cluster spin chains, which are of particular interest for numerical investigation. We identify field theories associated with these models, in addition to showing a way to calculate their ground state energies.

In chapter five, we will use the algorithm to examine the properties of the Ashkin-Teller and perturbed cluster quantum lattices at their phase transition. These results are important as they demonstrate the power

of the MERA to describe the ground states of a more complex class of models than have previously been examined. They also provide independent verification of the power and demonstrate the limitations of the numerical MERA. We will analyse these results, and describe how they allow us to link a particular field theory to the lattice models being considered.

The final chapter will discuss the results obtained from the MERA code, and the impact of the modifications. We conclude by discussing some possible future work.

1.1 Terminology and Formalism

Here, we present a brief overview of terminology which will be necessary for this thesis. For a more expansive look at the field of quantum information, please see [11].

A pure state of a quantum system is described by a ket vector $|\psi\rangle$ in a Hilbert space $\mathcal{H}$, a vector space of dimension d over the complex numbers. If the precise state of a system is unknown, a density matrix description can be used. If there is a probability p_j that the state is $|\psi_j\rangle$, then the density matrix is defined as $\rho = \sum_j p_j |\psi_j\rangle \langle\psi_j|$.

The density matrix has $\mathrm{Tr}\,\rho = 1$ (where Tr denotes the trace), which is a statement that the probability that the system is in some state is one. The square of the density matrix does not necessarily have trace 1. Those which do not are known as mixed states. These can be simply thought of as statistical distributions over pure states. There is no basis in which this class of states may be expressed as a single ket, so no change of basis renders them pure. If a pure state is defined on a combined system $|\psi\rangle \in \mathcal{H}_1 \otimes \mathcal{H}_2$, where $\otimes$ denotes the tensor product, then the reduced state on either of the component subsystems is not necessarily pure. The reduced density matrix on subsystem 1 is $\rho_1 = \mathrm{Tr}_2(|\psi\rangle \langle\psi|)$, where $\mathrm{Tr}_j(\cdot)$ is the partial trace over system j. This is clearly exemplified using a Bell state $|\psi\rangle = \frac{1}{\sqrt{2}}(|0\rangle |1\rangle + |1\rangle |0\rangle)$. The reduced density matrix on system 1 is then

$$\rho_1 = \mathrm{Tr}_2 \left(\frac{(|0\rangle |1\rangle + |1\rangle |0\rangle)(\langle 0| \langle 1| + \langle 1| \langle 0|)}{2} \right) = \frac{|0\rangle \langle 0| + |1\rangle \langle 1|}{2}. \tag{1.1}$$

This is a mixed state, since $\mathrm{Tr}(\rho_1^2) = 1/2$.

If the subsystems 1 and 2 are entangled, then the reduced state on either system will be mixed. By an entangled state, we mean a state which cannot be written as a product of pure states in the two Hilbert spaces. That is a state which cannot be written as

$$|\psi\rangle = |\psi_1\rangle \otimes |\psi_2\rangle \text{ such that } |\psi_1\rangle \in \mathcal{H}_1, |\psi_2\rangle \in \mathcal{H}_2. \tag{1.2}$$

States which can be written in the form of eqn. 1.2 are known as product states.

The Pauli matrices will be used throughout. These are a basis for operators on spin-$1/2$ systems, and are defined by

$$\begin{aligned} I &= |0\rangle \langle 0| + |1\rangle \langle 1|, & X &= |0\rangle \langle 1| + |1\rangle \langle 0|, \\ Y &= -i |0\rangle \langle 1| + i |1\rangle \langle 0|, & Z &= |0\rangle \langle 0| - |1\rangle \langle 1|, \end{aligned} \tag{1.3}$$

where $|0\rangle$ and $|1\rangle$ are orthogonal basis states often associated with spin up ($|\uparrow\rangle$) and spin down ($|\downarrow\rangle$).

1.2 Lattice Models

When considering many body systems, the standard example is the ideal gas. This is easy to analyse, and perturbative corrections allow for a more realistic model to be constructed. Far more interesting are the strongly interacting systems. These model a wide range of physical systems, in particular various phenomena in condensed matter physics. An important class of strongly interacting quantum many body systems are the spin lattice models. These are quantum spins of dimension d placed on some D dimensional lattice [12, 13]. These systems are commonly described by a Hamiltonian with coupling between nearest and next nearest neighbour sites on the lattice. As such, these are *local* models; the operators in the Hamiltonian only act locally on a small number of spins. The range of physical systems which can be modelled using spin lattices is vast, from quantum magnets to high temperature superconductors and gases of free particles [14–16].

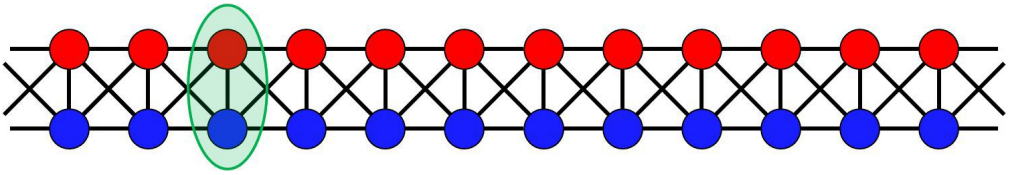

Figure 1.2.1 : We can think of the Ashkin-Teller model as being defined on a pair of parallel chains. The σ operators act only on the red chain and the τ act only on the blue. The lines represent coupling present in the Hamiltonian. The green region indicates a single site.

1.2.1 The Ising model

The canonical example of a quantum lattice is the spin-1/2 ($d = 2$) transverse field Ising model on a $D = 1$ chain (fig. 1.3.1 (a)), described by the Hamiltonian

$$H_{Ising} = J \sum_{j=1}^{N-1} X_j X_{j+1} + h \sum_{j=1}^{N} Z_j \tag{1.4}$$

where X and Z are the Pauli operators, and j denotes the site number on the N site chain. This model can describe a ferro or antiferromagnet depending on the sign of the coupling parameter J. h controls the strength of a transverse magnetic field [17]. This model then has two competing interactions. The ferromagnetic (antiferromagnetic) coupling term causes the spins to align (antialign) with their neighbours along the X axis. The field causes the spins to tend to align along the Z axis. When the strength of the two terms becomes equal ($|h| = |J|$), the system experiences a quantum phase transition [18]. This is a zero temperature phase transition, but has observable effects at nonzero temperatures [19]. At this *critical point*, correlations change from decaying exponentially with distance to obeying a power law. This increased correlation range makes these systems particularly resistant to numerical analysis. The Ising model can be exactly solved using a Jordan-Wigner transform [19], making it the workhorse model for benchmarking numerical algorithms designed to approximate the solution to quantum many body systems.

One of the most interesting, novel and unintuitive features of quantum systems is entanglement (defined above). Many lattice models have highly entangled ground states, including the antiferromagnetic Ising chain. The entanglement in some of these systems can be used as a resource for measurement based quantum computation (MBQC).

1.2.2 The Ashkin-Teller model

The Ising model is a very simple model. It has an immensely simple phase diagram, possessing only critical points. To describe real systems, we need to be able to construct and understand more complex models. In this section we describe another spin chain; the Ashkin-Teller model. The investigation of this lattice using the MERA algorithm described in chapters 2 and 3 is one of the key aims of this project, as it has a complex phase structure allowing for critical lines. These are lines in the phase diagram along which the model remains at a phase transition.

If we take a pair of Ising chains and couple them with a four spin interaction, we obtain the Ashkin-Teller (AT) model. This spin chain has spawned much interest since it was first defined in both its classical [20] and quantum [21] forms. There is a vast quantity of theoretical literature on the subject of its complex phase structure [22–26], and it has also been used to describe physical systems, including thin films [27], superconductors [28] and anyonic systems [29].

The Hamiltonian for this system is

$$H_{AT} = -\sum_{j=1}^{N} \sigma_j^Z + \tau_j^Z + \lambda \sigma_j^Z \tau_j^Z + \beta \left(\sigma_j^X \sigma_{j+1}^X + \tau_j^X \tau_{j+1}^X + \lambda \sigma_j^X \tau_j^X \sigma_{j+1}^X \tau_{j+1}^X \right) \tag{1.5}$$

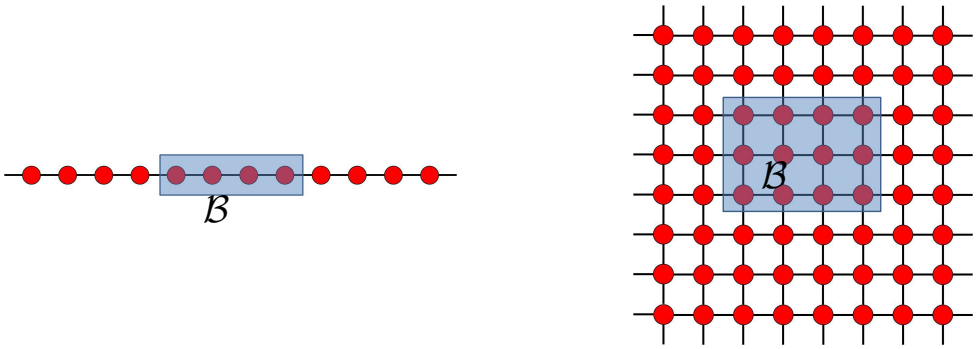

a) $D = 1$ spin chain b) $D = 2$ lattice

Figure 1.3.1 : Examples of lattices. The entanglement entropy of gapped local model obeys an area law. In 1D this is constant, and in 2D is proportional to the perimeter of the block $\mathcal{B}$ (blue region). Critical models in 1D have a logarithmic correction to this area law.

where $\{\sigma^X, \sigma^Y, \sigma^Z\}$, $\{\tau^X, \tau^Y, \tau^Z\}$ are two sets of mutually commuting Pauli operators, that is they obey the usual Pauli relations within a set and

$$[\sigma_j^{X,Y,Z}, \tau_k^{X,Y,Z}] = 0, \tag{1.6}$$

for all j, k. We think of these as acting on two different chains, as in fig. 1.2.1. Each site j contains a pair of spin $1/2$ particles, one red and one blue.

1.3 Entanglement Entropy

The entanglement in the ground state of a many body system can be quantified using the block entanglement entropy. This is defined using the Von Neumann entropy, and measures the entanglement between a block $\mathcal{B}$ and the rest of the chain. The entanglement entropy is defined as

$$S(\rho_{\mathcal{B}}) = -\operatorname{Tr}(\rho_{\mathcal{B}} \log \rho_{\mathcal{B}}), \tag{1.7}$$

where $\rho_{\mathcal{B}}$ is the reduced density matrix on a block, obtained by tracing out the rest of the system [30]. For gapped systems, this can be shown to obey an area law [31]. The entanglement entropy between a block and the rest of the lattice is proportional to the area of the boundary of the block. In 1D, the entanglement entropy is bounded by some constant since the area is always the same, then

$$S_{gapped} \leq \frac{c}{3} \log_2(\xi/a) + k, \tag{1.8}$$

where c is the central charge from the associated conformal field theory, which we explain in section 1.4. ξ is the correlation length, a is the lattice spacing and k is a universal constant. In 2D, the area is proportional to L, the side length of the block so $S \leq \alpha L$, for some constant α as shown in fig. 1.3.1.

The area law is violated for critical systems due to the diverging correlation length. In this case, the area law has a logarithmic correction, so in 1D, the entropy scales as

$$S_{critical} \leq \frac{c}{3} \log_2(L/a) + k, \tag{1.9}$$

where L is the length of $\mathcal{B}$ [31, 32].

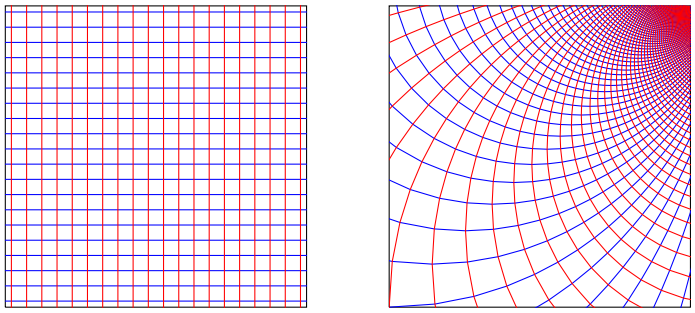

Figure 1.4.1 : The action of the special conformal transformation on a square grid.

1.4 Conformal Field Theories

The continuum limit of a lattice is described by a field theory. For example, a lattice of quantum harmonic oscillators becomes a QFT of noninteracting bosons as the lattice spacing goes to zero. Since a critical lattice model is scale invariant, the thermodynamic limit is described by a scale invariant field theory, known as a conformal field theory (CFT) [33]. The Ashkin-Teller model is thought to be described by a particular bosonic CFT. Investigating this field theory, via its correspondence to the lattice model will form a key part of this thesis. In particular, much of the physical data we extract from the MERA corresponds to the data required to construct a CFT, so we briefly review these theories here.

CFTs are quantum field theories which are invariant under the action of the conformal group; the group of transformations on the underlying spacetime which preserve angles [33–35]. This includes the Poincaré transformations

$$x'^{\mu} = x^{\mu} + a^{\mu} \qquad \text{(Translations)}$$
$$x'^{\mu} = \Lambda^{\mu}{}_{\nu} x^{\nu} \qquad \text{(Lorentz Transformations)}$$

which describe the isometries of Minkowski spacetime, and the added transformations

$$x'^{\mu} = \lambda x^{\mu} \qquad \text{(Scaling Transformations)}$$
$$x'^{\mu} = \frac{x^{\mu} - b^{\mu} x^2}{1 - 2b\dot{x} + b^2 x^2} \qquad \text{(Special Conformal Transformations)}$$

The special conformal transformation (SCT) can be reinterpreted as an inversion ($x'^{\mu} = \frac{x^{\mu}}{x^2}$) followed by a translation and another inversion. The action of this transformation on a square grid is shown in fig. 1.4.1. In D = 2, the constraints of conformal invariance impose very strict limitations of the field content of the CFT. The Hilbert space breaks into representations of the Virasoro algebra [33]. Here, we have an infinite set of operators $L_n, \bar{L}_n$ ($n \in \mathbb{Z}$), which act in a similar way to bosonic creation and annihilation operators $a^{\dagger}, a$ from quantum field theory. The vacuum is defined such that

$$L_n |0\rangle = 0 = \bar{L}_n |0\rangle \qquad \forall n > -1. \tag{1.10}$$

Each representation is then labelled by a primary field $\phi_{h,\bar{h}}$ [35], which has associated state

$$|h, \bar{h}\rangle = \phi_{h,\bar{h}} |0\rangle . \tag{1.11}$$

These primaries are quasivacuum states, since they are annihilated by $L_n(\bar{L}_n)$ for $n > 0$. These are in analogy to the usual vacuum state from quantum field theory. They are eigenstates of $L_0(\bar{L}_0)$ with eigenvalues $h(\bar{h})$ such that

$$(L_0 + \bar{L}_0) |h, \bar{h}\rangle = (h + \bar{h}) |h, \bar{h}\rangle \tag{1.12}$$
$$(L_0 - \bar{L}_0) |h, \bar{h}\rangle = (h - \bar{h}) |h, \bar{h}\rangle . \tag{1.13}$$

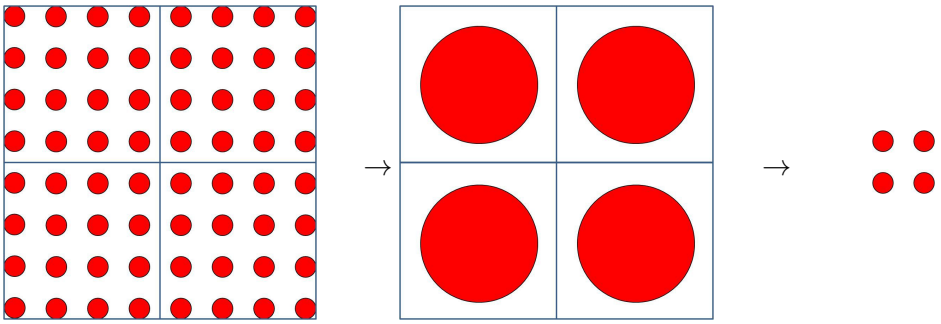

a) First the lattice is divided into blocks

b) The spins are replaced with a single effective spin

c) Finally the lattice is rescaled

Figure 1.5.1 : Examples of lattices. The entanglement entropy of gapped local model obeys an area law. In 1D this is constant, and in 2D is proportional to the perimeter of the block $\mathcal{B}$ (blue region).

$L_0+\bar{L}_0$ is the infinitesimal generator of scaling transformations, so we identify $h+\bar{h}$ as the scaling dimension [34]. The name 'dimension' arises from classical field theory, where these quantities can be calculated via dimensional analysis. By interpreting the CFT as acting in (1+1) dimensions, that is one time and one space, we can interpret the rescaling as evolution under the Hamiltonian $L_0 + \bar{L}_0$. Acting with $L_{-n}(\bar{L}_{-n})$ adds n units of energy, creating a descendent of $|h, \bar{h}\rangle$ with energy $h+\bar{h}+n$. The degeneracy of the states increases exponentially as we increase n, since there are two ways to add a single unit $(L_{-1}, \bar{L}_{-1})$, five ways to add two units $(L^2_{-1}, \bar{L}^2_{-1}, L_{-1}\bar{L}_{-1}, L_{-2}, \bar{L}_{-2})$ and so on. Since $i(L_0 - \bar{L}_0)$ generates rotations, we call $h - \bar{h}$ the 'spin' number s. Knowledge of Δ and s allows for recovery of h and $\bar{h}$. The commutation relations of L_n are

$$[L_n, L_m] = (n-m)L_{n+m} + \frac{c}{12}n(n^2-1)\delta_{n+m,0}, \tag{1.14}$$

defining the Virasoro algebra [36] ($\bar{L}_n$ obeys the equivalent relation). The central charge c arises in the quantum case only, and can be interpreted as the Casimir energy, arising from quantisation on the cylinder [33].

The conformal field theory can be completely determined by knowledge of the primary fields $\phi_{h,\bar{h}}$, the central charge and the operator product expansion (OPE) coefficients, which describe the result of bringing two fields to the same location [35]. For $c < 1$, there exists a complete classification of the unitary CFTs (CFTs for which probability is conserved). Here, the field content can be completely determined by imposing that all the states have nonnegative inner-product, which also means $h, \bar{h} \geq 0$ [37]. The CFTs corresponding to the models described in this thesis, includeing the Ashkin-Teller model are $c = 1$ theories, and are more complex in structure.

Later, we will show how the scaling dimensions $\Delta_\phi = h + \bar{h}$ and central charge, properties of a field theory, can be extracted from the MERA simulations of the lattice models.

1.5 Renormalisation and the Renormalisation Group

At criticality, lattice models become scale invariant; there is no characteristic length scale since the correlation length becomes infinite. One of the main tools used to investigate how physics changes on different length scales is the Renormalisation Group (RG) techniques developed by Wilson [38]. The elementary RG transformation on a lattice is easily understood for a classical magnet, and is summarised in fig. 1.5.1 (a)-(c). At the microscopic scale, we have a lattice of classical spins [39]. The spins can be blocked together, and replaced by an effective spin, using, for example, a majority vote or average spin. The system can then be rescaled. This process has removed some of the degrees of freedom and replaced the lattice by some effective lattice, described by a new Hamiltonian, with a new scale [40]. If the lattice is unchanged under this action, then the model is scale invariant.

The RG transformation generates flows in parameter space, with scale invariant systems corresponding to the fixed points of the flows [41] since they are unchanged under renormalisation. Perturbations added to the Hamiltonian may be *relevant*, *marginal* or *irrelevant* [41–43]. Relevant perturbations grow under rescaling, so affect the macroscopic physics. Irrelevant perturbations flow back to the fixed point, so do not affect the thermodynamic properties. Marginal terms neither flow towards or away from the fixed point, but remain equally important at all scales. Critical systems correspond to unstable fixed points since they have relevant operators. The different types of perturbation are easily identified in the $D+1$ dimensional CFT corresponding to the D dimensional scale invariant lattice. Marginal operators are those with $\Delta = h + \bar{h} = D + 1$, relevant operators are those with $\Delta < D + 1$, and operators with $D + 1 < \Delta$ are irrelevant [42]. In this thesis, we are interested in the thermodynamic properties of quantum spin chains, and so will only consider relevant and marginal operators.

In this chapter, we have introduced some of the formalism and physical concepts required for this thesis. In particular, we have introduced lattice models; the central focus of this research. We have also introduced conformal field theories, which describes the thermodynamic limit of these spin chains, and who's building blocks we will extract from our numerical investigations.

Chapter 2

Tensor Networks

Tensor networks are used to describe the properties of quantum systems which possess some notion of locality. They are particularly useful for examining the ground state of many body systems, where they can be used both as an analytical tool and a numerical ansatz, allowing exact solution and accurate approximation [44].

In this chapter, we will describe tensor networks, with a particular focus on a network first proposed in 2007 [1]. This is known as the multiscale entanglement renormalisation ansatz (MERA), a tool for investigating the macroscopic physics of critical quantum systems. We will review a general algorithm first described in 2009 [2], used to optimise the network to efficiently represent the ground state of this class of models. We will also provide the methods used to extract conformal data from a well converged MERA. These ideas for the basis for our new algorithm, and the code to implement it.

We begin by describing a standard notation used to describe and manipulate tensor networks [13,45].

2.1 Introduction to tensor network formalism

A wide variety of tensor networks have been proposed, including matrix product states (MPS) [46] and its generalisation, projected entangled pair states (PEPS) [47]; tensor tree networks (TTN) [48]; and the multiscale entanglement renormalisation ansatz (MERA) [1] to name just a few. These are all based on decompositions of an n index tensor, with the choice of dummy indices defining the different networks. Due to the complexity of the decomposition, a graphical notation is usually used, allowing the connectivity of the network to become transparent.

The wavefunction of the ground state of an n site system of d dimensional spins is written in the product basis as

$$|\psi\rangle = \sum_{i_1=1}^{d} \cdots \sum_{i_n=1}^{d} c_{i_1 \cdots i_n} |i_1\rangle \otimes \cdots \otimes |i_n\rangle \,. \tag{2.1}$$

The tensor $c_{i_1 \cdots i_n}$ then contains all the information about the system. This tensor is can be written in a graphical notation as

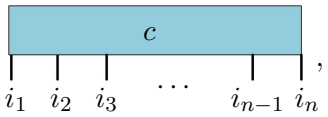

, (2.2)

with a leg for each index.

We can use this notation to make transparent a range of tensorial operations, such as matrix multiplication. A matrix is a two index tensor, and the product of two matrices can be written

$C_a^d = A_a^b B_b^d \Leftrightarrow$ 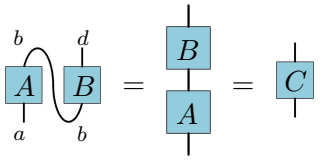

. (2.3)

Here, the b index is common, so is summed over. In the graphical form, any index connected to a pair of tensors is implicitly summed over, as in the Einstein convention.

We can use this notation to perform more complex operations, such as the tensor product

$$A_a^b B_c^d = C_{ac}^{bd} = \quad = \quad , \tag{2.4}$$

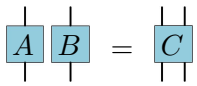

the partial trace

$$C_{ab}^{db} = \quad = \quad , \tag{2.5}$$

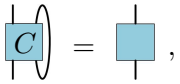

and singular value decomposition (SVD)

$$M = VSW^\dagger = \quad = \quad , \tag{2.6}$$

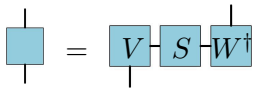

where V and W are unitary, and S is positive and diagonal. This is a particularly useful decomposition, which is frequently used in the study of highly entangled systems [49, 50]. The entries of S are the singular values. In contrast to the eigenvalue decomposition, the SVD can be applied to all matrices, both square and rectangular.

In the framework used here, upper and lower indices can be exchanged freely, though Hermitian conjugation must be applied. This is clear in the case

$$|x\rangle = \quad \rightarrow \langle x| = \quad . \tag{2.7}$$

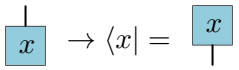

With this notation, we can decompose eqn. 2.2 in many different ways, leading to the idea of a tensor network. One of the simplest decompositions is the matrix product state (MPS), obtained by sequential singular value decompositions

$$= \quad , \tag{2.8}$$

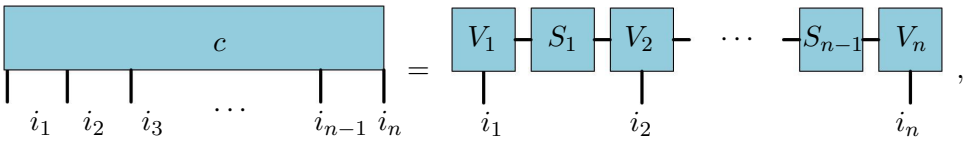

where the vertical 'free' indices have the dimension of the physical spins d, and the internal 'dummy' indices have dimension χ, known as the bond dimension.

2.2 Matrix Product States

An MPS is simply a different way of writing $c_{i_1 \cdots i_n}$ (eqn. 2.2). In particular, if we contract all the internal indices, we recover the full description of the system. The amount of information, and thus the size of $c_{i_1 \cdots i_n}$, required to describe the ground state of an N body quantum system is exponential in N, however most of the values in the S tensors are vanishingly small when we restrict to physical states [51]. Thus, if we truncate the dimension of the bonds (dummy indices) in such a way as to only discard small values, our description will efficiently approximate the ground state. That is, it will provide a description which is at most polynomial in N, but which retains the essential physics of the full description.

The amount of entanglement that can be represented in a tensor network is related to the bond dimension. The sum of the dimensions of all the bonds which would have to be broken to detach a block from the rest of the diagram is proportional to the total entanglement between the block and the rest of the network which can be captured by the network. For an MPS, this is simply 2χ regardless of the block size. This is the same relation as the entanglement entropy scaling in the ground state of a gapped one dimensional system [52]. It can be shown that the ground state of every gapped spin chain can be approximated to a given accuracy with bond dimension *linear* in N [51, 52]. The remaining problem is to find a suitable truncation.

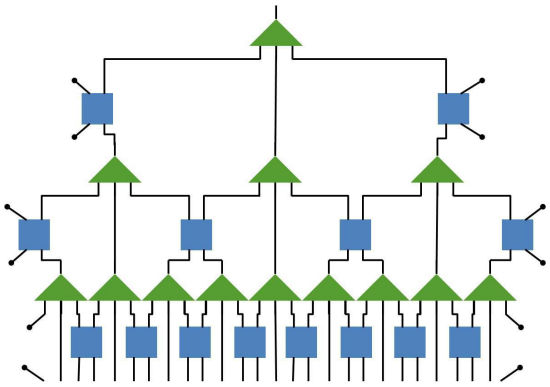

Figure 2.3.1 : The decomposition known as the MERA. This is a more highly connected diagram than the MPS, meaning much more highly entangled states can be represented.

There is a small set of models for which an exact MPS description can be written down, however for most systems we require a numerical algorithm to choose the correct tensors for an accurate approximation. To be useful, this algorithm should be able to find the ground state in a computationally *efficient* way. In other words, the resources (time and memory) should scale at most polynomially with the system size. One of the most common algorithms for MPS optimisation is time evolving block decimation [53–55]. This begins with a random MPS, and simulates evolution in imaginary time. This acts as time evolution of a dissipative system [56], under which it should relax to its ground state, and thus the tensors tend towards a good representation of the ground state (assuming a sufficiently large bond dimension has been chosen).

Although the class of models which can be efficiently approximated efficiently using an MPS description is large, it excludes the most interacting states. In particular, quantum critical states cannot be represented due to the divergence in the correlation length leading to a logarithmic violation of the area law. These systems have no classical counterpart, and thus give us the most exciting and novel physics. Although modifications to the MPS have recently been proposed, such as incorporating finite size scaling techniques to allow for MPS investigation of these models [57, 58], a more natural decomposition exists which allows these models to be analysed directly. This is known as the multiscale entanglement renormalisation ansatz.

2.3 Multiscale Entanglement Renormalisation Ansatz

One of the decompositions which are collectively known as the multiscale entanglement renormalisation ansatz (MERA) [1] is shown is fig. 2.3.1. The particular form described here is the ternary or $3:1$ scale and translationally invariant MERA.

This diagram is much more highly connected than that of the MPS. Due to the layered structure, the minimum number of bonds that must be broken to detach any block increases logarithmically with the block size, exactly the logarithmic correction to the area law seen in critical spin chains. As such, the MERA is expected to be able to efficiently represent this wider class of systems.

With so many tensors in the network, how do we design an algorithm to optimise for an accurate ground state representation? We can enforce spatial symmetries present in the model of interest, restricting our choice of tensors. Many spin chains are defined by a translationally invariant local Hamiltonian. It is reasonable to expect that the ground state will reflect this invariance. In addition, critical systems are scale invariant. The MERA has a clear layered structure, with each layer interpreted as describing the system on a different length scale. As such, both the microscopic and macroscopic physics is captured by a well converged MERA. Translational invariance can be imposed by making all tensors identical within a given layer, and scale invariance by making all layers identical. As such, we reduce the problem to selecting a pair of tensors, u (blue squares in the diagram) and w (green triangles).

2.3.1 Enforcing Locality in the MERA

One of the most important assumptions in physics is that of locality. This is the axiom that events at x only affect regions in the region directly around it. The couplings described in the Hamiltonian for the Ising model (eqn. 1.4) are local, and we expect them to remain local upon renormalisation. In order to enforce this, we will make an assumption regarding the form of the tensors, and show how this causes locality to be preserved on all scales. Let the tensors u and w have the properties

$w^\dagger w = I \equiv$ 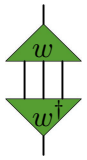 (2.9)

$uu^\dagger = u^\dagger u = I^{\otimes 2} \equiv$ 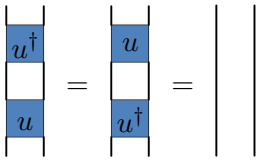 (2.10)

If we then include a local operator acting on a pair of sites on layer L and calculate the expectation value $\langle\psi|\,\hat{O}\,|\psi\rangle$, we can apply these contraction rules and see that it indeed remains local on layer $L+1$.

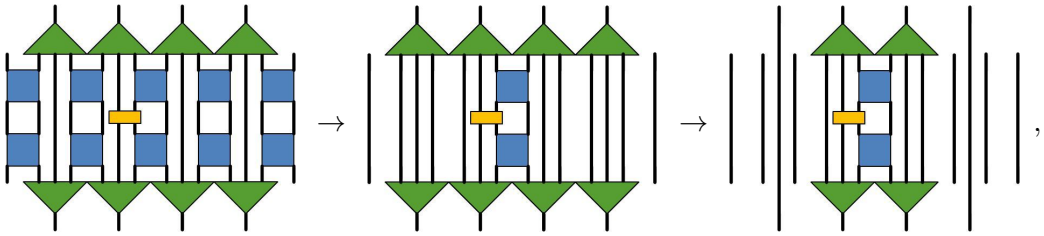 (2.11)

where the yellow rectangle is some local operator. This operator only affects a pair of sites on the coarse grained layer, and has therefore remained local.

Removing the operator from the contracted network, we obtain an *ascending superoperator*,

$A_L(\cdot) =$ 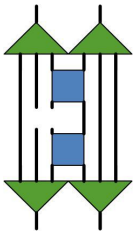 , (2.12)

which takes a local operator on layer L to a local operator on layer $L+1$. We can then use this superoperator to create an effective Hamiltonian on each layer, given some physical Hamiltonian on layer $L = 0$. The reduced density matrix, describing the state of a pair of spins on layer L can be obtained from that on layer $L+1$ using the operator dual to A, know as the descending superoperator, and drawn as

$D_L(\cdot) =$ 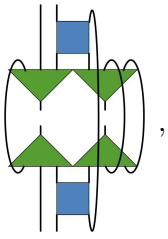 , (2.13)

where the tensor to be lowered is inserted in the middle.

2.3.2 Isometric Tensors and Renormalisation

The tensors u are required to be unitary by eqn. 2.10 [11]. This is simply the requirement that if states are acted upon by u, properly normalised states are the result; probability is conserved. The condition on w is somewhat weaker, only enforcing the isometric constraint $w^\dagger w = I$. $w^\dagger$ is a map

$$w^\dagger : \mathcal{H}_{\text{in}}^{\otimes 3} \to \mathcal{H}_{\text{out}}, \tag{2.14}$$

from the input space with three legs to the output space with just one. This corresponds to making an effective spin from the three input spins. Clearly, if $d_{\text{out}} = d_{\text{in}}^3$, all degrees of freedom can be retained. However, as in the MPS above, we can choose to truncate the dimension d_{out} of $\mathcal{H}_{\text{out}}$, so that $d_{\text{out}} < d_{\text{in}}^3$. This truncation and rescaling is exactly the operation described in sec. 1.5 for the renormalisation group transformation. The unitary operator can be interpreted as removing the entanglement at the edges of the blocks, preventing build-up which causes the size of the Hilbert space to grow when RG is applied to entangled quantum systems [1]. In this way, the MERA is an entanglement renormalisation scheme, allowing renormalisation techniques to be extended to a huge class of highly entangled states. The aim of any optimisation algorithm is then to choose the tensors such that they best retain the low energy degrees of freedom, and truncate away only the high energy subspace.

2.4 Optimisation Algorithm

Here, we will describe the basic algorithm used to update the tensors in the MERA following [2–5]. This allows convergence towards a network which faithfully represents the ground state of a given Hamiltonian. This algorithm can be carried out in a computationally efficient way as a result of the isometric constraint on the tensors described above (eqns. 2.9 and 2.10). Any network which uses isometric tensors to enforce locality in this way is an example of a MERA. Here, we consider the ternary MERA, which uses 3:1 tensors. In particular, we will specialise to the case of a scale and translationally invariant model.

2.4.1 Updating Tensors

The optimisation proceeds using structures known as *environment* networks. These are fully contracted networks containing the effective two site Hamiltonian (orange rectangle) on layer L and the reduced density matrix on a pair of sites on layer $L+1$ (purple rectangle).

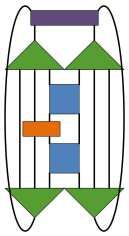

(2.15)

We can view this network as an ascending superoperator, giving h_{L+1}, followed by $\text{Tr}(\rho_{L+1}h_{L+1})$. It is then clear that this computes the energy of the state on layer $L+1$. We wish to minimise this energy, however this network is quadratic in the tensors u and w, meaning that it contains both u and $u^\dagger$, w and $w^\dagger$. No algorithm exists to optimise this network whilst also retaining the unitary constraint, so we optimise a linearised network instead [2,4]. This is the network created by removing the tensor to be optimised from the network, and temporarily assuming that $u^\dagger$ is unrelated to u. The environment of u is computed by removing u from the network, leaving

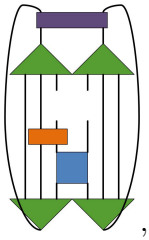

, (2.16)

which can be contracted to give a four index tensor E_u. The energy is given by the contraction of this network with u, so

$$E = \text{Tr}(E_u u). \tag{2.17}$$

By assuming u and $u^\dagger$ are independent tensors, we can use a result from linear algebra to minimise this trace. We can decompose E_u using a singular value decomposition, to give

$$E_u = VSW^\dagger. \tag{2.18}$$

Using a result from matrix analysis [59], we can minimise eqn. 2.17 by setting

$$u' = -WV^\dagger. \tag{2.19}$$

Calculating the analogous environment for w, we can use the same process to update all tensors in the network.

The superoperators described here correspond to one particular choice of location for h and ρ. In reality there are three different locations, and we use the average superoperators

$A(h) = \frac{1}{3}$ 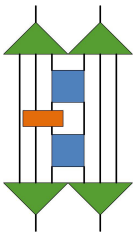 $+ \frac{1}{3}$ 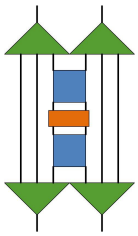 $+ \frac{1}{3}$ 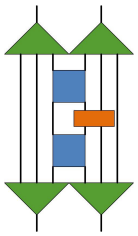 , (2.20)

and

$D(\rho) = \frac{1}{3}$ 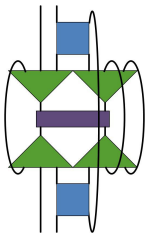 $+ \frac{1}{3}$ 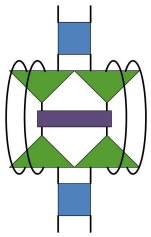 $+ \frac{1}{3}$ 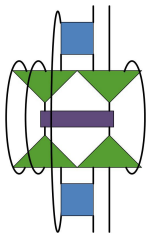 . (2.21)

2.4.2 Optimisation of the Network

2.4.2.1 Noncritical Systems

Gapped models do not possess scale invariance, so each layer in the MERA must be distinct. With the knowledge of how to optimise each tensor, we need an algorithm to update the entire network. In particular, we initially only know the Hamiltonian on the zeroth (physical) layer h_0, so cannot update the higher layers without first ascending it. However, we cannot optimise the bottom layer without a reduced density matrix on layer one. Thus, an alternating algorithm is used. Initially, a guess is made to the reduced density matrix on the very top layer. This is then lowered through each layer using the appropriate descending operator (formed from the tensors $\{u_L, w_L\}$ from layer L. We now have the tensors required to update the lowest layer, so this proceeds as above. Once this is done, h_0 can be ascended, meaning the next layer can be updated also (the full set of reduced density matrices was stored on the way down). This process proceeds until all layers have been updated, and is then repeated until the MERA stops changing to within some tolerance.

2.4.2.2 Scale Invariant MERA

The scale invariant MERA has an infinite number of layers, otherwise there would be a length scale upon which the state disappeared. Despite this, there are only a pair of tensors $\{u, w\}$ to be updated, since all layers should be identical. The density matrix used should be the same on all layers, and is know as the *fixed point* density matrix, ρ_{fp}. By the construction of the MERA, D (eqn. 2.21) is a quantum channel. That is, it preserves the trace of the density matrix and the eigenvalues obey $|\lambda_n| \leq 1$ [60]. Then, the unique operator fixed by D is ρ_{fp}. All other operators decay under many applications of D. Thus, we do not have to calculate the density matrix on each layer, rather, we simply need to find the fixed point of D. As described above,

the purpose of the MERA is to provide a computationally tractable way of approximating the ground states of quantum systems. As such, the algorithm is designed to be as efficient as possible. In appendix A, we demonstrate how the optimal contraction scheme of a particular network depends on the particular structure. By contraction scheme, we mean the order in which the contraction is carried out, i.e. which indices are contracted first, second etc. This is explained in detail in appendix A. The contraction of $D(\rho)$ scales as χ^8, whereas the construction of $D(\cdot)$ scales as χ^{10}. In practice then, ρ_{fp} is found by applying D several (around 10 appears to work, although this can be decreased as the MERA converges) times rather than calculating the eigenspectrum of D.

The Hamiltonian is not a fixed point of A, rather the identity operator is [61]. This is clear by inserting the identity tensor into $A(\cdot)$ above and applying the unitary constraints (this is also the reason for the presence of the operator with eigenvalue 1 of D above). As such, we cannot find a fixed point Hamiltonian. Since the network is linear in h, we can use the average Hamiltonian

$$\bar{h} = \sum_{L=0}^{\infty} \frac{1}{3^L} h_L \tag{2.22}$$

to capture the scale invariant nature of the network. The $1/3^L$ factor is a consequence of the relative number of tensors on subsequent layers. Clearly we cannot calculate this infinite sum efficiently, however due to the rapid decay we only need to calculate the first few terms. We find that 10 is sufficient. Once the network is well converged, we use

$$\bar{h} = h_0 + \frac{1}{3} A(\bar{h}), \tag{2.23}$$

where $\bar{h}$ is the average Hamiltonian from the previous iteration. Since the Hamiltonian should be the same on all layers up to a numerical factor, this accurately approximates the infinite sum above. We then use $\{\rho_{fp}, \bar{h}\}$ to update $\{u, w\}$ by computing the environments as described above. Thus, the algorithm for the scale invariant MERA has only two steps,

1. Using $\{u, w\}$, compute ρ_{fp} and $\bar{h}$,
2. Using $\{\rho_{fp}, \bar{h}\}$, update u and w.

These are repeated until the MERA is well converged.

2.4.2.3 Choosing χ

The above algorithm requires all the w tensors to be identical. In particular, the upper and lower indices have the same dimension. Thus, all indices must carry the physical dimension of the spins. This corresponds to a large truncation initially, and tends to lead to poor MERA representations of the desired state. We need to use a slightly modified algorithm which allows freedom in the choice of χ. This can be achieved in two different ways, both of which we will use.

Preblocking Preblocking is the process of initially relabelling what we call a 'site' in the Hamiltonian. A pair of spins of dimension d are combined into a single site of dimension d^2. As such, we can choose χ to be a power of the physical dimension. This process is lossless; it does not involve any truncation. The new Hamiltonian is calculated from the original by blocking pairs of sites into a single new site using

$h_{eff} = \frac{1}{2}$ 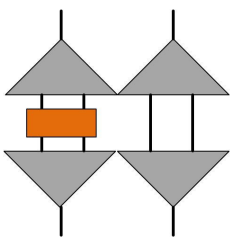 $+$ 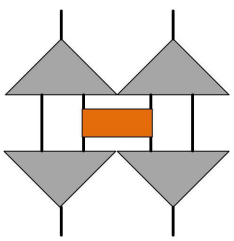 $+ \frac{1}{2}$ 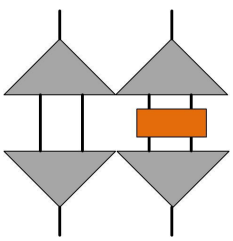 , (2.24)

where the coefficients arise from the fact that the leftmost diagram is the rightmost diagram in the site shifted one to the left. The dimension of the upper index is d^2, and these are identity tensors.

Preblocking can be extremely useful for models with low physical dimension (such as the Ising model with $d = 2$), allowing larger bond dimensions. It also allows for models which do not possess one spin translational invariance, but rather a longer range invariance, to be blocked to ones that do.

Due to the $d \to d^2$ mapping, if preblocking is performed multiple times, the effective physical dimension, and thus χ grows very rapidly, and quickly become intractable. To be able to choose χ more freely, we require another method to allow more freedom.

Translationally Invariant Layers Relaxing the scale invariant condition allows us to include a few layers with different tensors at the base of the MERA. These retain the translational invariance, so are named translationally invariant layers (TILs) as opposed to the scale invariant layers above. These layers each have a pair of tensors which must be optimised as above. Since they differ from the bulk, they can have arbitrary dimension on the upper indices, allowing for any choice of χ. Some experimentation is required to determine the correct number of TILs to include. Typically, one is used to select χ and the MERA is optimised. After, the bottom scale invariant layer is allowed to vary, giving more variational parameters and often an improvement in the output. Once this has converged, the new base scale invariant layer is allowed to vary and the new MERA is converged. This can be repeated until no improvement is seen in adding more TILs (usually after there are 2-3 TILs).

2.4.3 Computational Cost

The computational cost of the algorithm is an important consideration. To make the algorithm useful, it must be efficient. This means that the time and memory costs for increasing χ should scale at most polynomially. The cost of contracting a network is easily calculated for a particular contraction scheme. This involves contracting pairs of tensors in some order, and looking for the most costly contraction. This process is described in detail in appendix A. The time cost of a contraction is proportional to the total number of indices (both free and dummy) connected to the two tensors involved, with contracted indices being counted only once. Thus, eqn. 2.9 scales in time as χ^5 whilst eqn. 2.10 scales as χ^6. The memory cost is proportional to the highest rank tensor formed using the contraction scheme. The scaling in time for the ternary MERA scheme described here is χ^8 if the optimal contraction scheme is chosen [2]. Generically, however, the selection of the optimal scheme is #P-complete, and thus is intractable for a classical computer for sufficiently large networks.

2.5 Conformal Data from the MERA

Once the MERA is well converged, we wish to extract some physical information about the spin model. The thermodynamic limit of the model at its quantum phase transition is completely described by its associated conformal field theory. Here, we describe how the data necessary to construct the CFT can be extracted from the scale invariant MERA.

The isometric tensor in the MERA performs a rescaling transformation. As described above (section 1.4), $L_0 + \bar{L}_0$ is the generator of scaling transformations, with eigenvalues Δ_ϕ which are known as the scaling dimensions. By finding the eigenoperators of the one site scaling superoperator

$S(\cdot) =$  , (2.25)

we can find the scaling operators and their dimensions. Since S corresponds to a finite transformation, it is related to $\exp(L_0 + \bar{L}_0)$ (recall that $L_0 + \bar{L}_0$ is the infinitesimal generator of scaling transformations). The eigenvalues λ of S are then related to the scaling dimensions via $\Delta_\phi = \log_3(\lambda)$. The base 3 logarithm occurs since the isometries are $3:1$ tensors.

The central charge of the theory can be extracted from ρ_{fp} using the corrected area law (eqn. 1.9), repeated here

$$S_{critical} = \frac{c}{3}\log_2(L/a) + k, \tag{2.26}$$

where c is the central charge of the CFT, L is the block length, a is the lattice scaling (here, $a = 1$ by definition) and k is some constant. Then by calculating the entropy for one and two site blocks, we can calculate c by

$$\frac{c}{3} = \frac{c}{3}\log_2(2) + k - (\frac{c}{3}\log_2(1) + k). \tag{2.27}$$

The one site density matrix is calculated by symmetrising over the two ways of tracing out a subsystem from ρ_{fp}. With the scaling operators and their dimensions, as well as the central charge and the OPE coefficients, the CFT describing the thermodynamic limit of the lattice model can be completely classified. Thus, we can use the MERA to extract most of the conformal data, giving a complete classification of the CFT.

In this chapter, we have reviewed a basic algorithm which can be used to optimise the scale invariant MERA to approximate the ground state of a critical spin chain. We have also explained how physical information can be extracted from a well converged MERA, providing data to construct a CFT describing the continuum limit of the lattice. This algorithm can be modified by incorporating further physical knowledge about the particular models of interest, such as internal symmetries (e.g. invariance under spin flips) of the lattice Hamiltonian. The next chapter will describe how these constraints can be included to achieve a more accurate description of the ground state of interest. We will also describe some physically motivated approximations that can be added to improve the scaling of the algorithm with χ, the parameter which sets the accuracy of the tensor network description.

Chapter 3

Modifications to the MERA Algorithm

In the previous chapter, we described how the MERA can be optimised to describe the ground state of a quantum lattice models described by local Hamiltonians. We imposed the constraints of scale and translational invariance, and locality preservation. This allowed design of an algorithm which required optimisation of only a pair of tensors u and w. The optimisation was achievable in time that scaled as χ^8, where χ was the bond dimension of the MERA, the parameter which sets the accuracy of the converged network.

In this chapter, we will describe some novel modifications made to our MERA code. These both increase the efficiency of the algorithm, and impose physical constraints which are known to be present in the ground states of interest. Our alterations allow for both a decrease in the computation time by a multiplicative factor, and an improvement in the scaling of the algorithm.

We begin by describing how tensors may be selected to improve convergence times, and how we can make use of decay of correlations to improve the scaling of the algorithm. In the second half of this chapter, we describe how symmetries which are present in the Hamiltonians for the models of interest may be incorporated into the MERA. This has the effect of decreasing computational cost, and ensures that the ground states have the relevant symmetries.

3.1 Preprocessing

In the algorithm described above, the tensors are initially chosen randomly. The convergence of the MERA can be hastened, and the potential for erroneously finding local minima decreased by preconverging the tensors [62].

When constructing a MERA, we want to choose the u's and w's that retain only the low energy subspace. We aim to select which minimise $\mathrm{Tr}(\mathcal{M}^\dagger H \mathcal{M})$, where $\mathcal{M} =$  , since if this is minimised, the high energy subspace will be truncated preferentially.

It is clear that $\mathcal{M}^\dagger : \mathbb{V}^{\otimes N} \to \mathbb{V}^{\otimes N/3}$, since the renormalising tensors map three spins onto a single effective spin at the next length scale.

Recall that we imposed an isometric constraint on the tensors, so $\mathcal{M}^\dagger \mathcal{M} = \mathbb{I}_{N/3}$, which allows the minimisation problem to become

$$\min_{u,w} \mathrm{Tr}(\mathcal{M}^\dagger H \mathcal{M}) = \min_{u,w} \mathrm{Tr}(\mathcal{M}^\dagger H \mathcal{M}\mathcal{M}^\dagger \mathcal{M}) = \min_{u,w} \mathrm{Tr}(\mathcal{M}\mathcal{M}^\dagger H \mathcal{M}\mathcal{M}^\dagger). \tag{3.1}$$

In this form, we can identify $\mathcal{M}\mathcal{M}^\dagger$ as a projector

$$\mathcal{M}\mathcal{M}^\dagger = \mathcal{P} : \mathbb{V}^{\otimes N} \to \mathbb{V}^{\otimes N/3} \to \mathbb{V}^{\otimes N}. \tag{3.2}$$

So, minimising over u and w allows projection onto the low energy subspace of the Hamiltonian. Temporarily neglecting the upper layers of the MERA for numerical convenience, we can use this to design an algorithm to preprocess the tensors. By using several layers, we can form the projector by connecting the upper free legs as fig. 3.1.1. Alowing us to update the layers in pairs, so each is minimised in the presence of the others. The tensors are optimised in the standard way. This is repeated until a certain level of convergence is realised, then the main MERA algorithm is used, with these tensors as a start point.

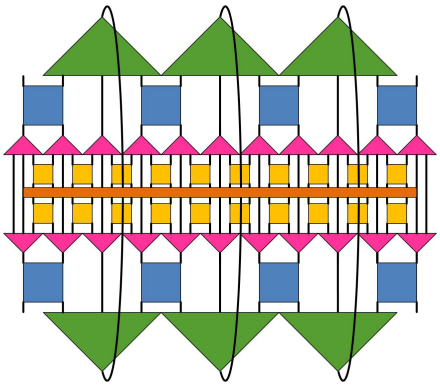

Figure 3.1.1 : The diagram used to preprocess the tensors to give an initialisation state which lives in the low energy subspace of the Hamiltonian. Here, the inner layer is coloured differently to indicate it is a TIL, included to allow choice of χ. The orange rectangle indicates the Hamiltonian.

By preprocessing the first two layers in this way, we can achieve part of the convergence without the need to calculate objects such as the fixed point density matrix and average Hamiltonian, both of which are computationally expensive.

3.2 Reducing Computational Cost

The algorithm described above requires contraction of the ascending and descending superoperators, as well as the environments of u and w. It can be shown (appendix A) that the time for this scales as χ^8. This rapidly becomes computationally intractable, so further approximations are necessary. Two are described in this thesis.

3.2.1 χ_L and χ_U

The disentangler u described above obeys a unitarity constraint. If we relax this, and allow the upper and lower indices to differ in dimension, so we now have two bond dimensions χ_L and χ_U for the lower and upper indices. The role of the two tensors becomes somewhat blurred. We retain an isometric constraint on u, so the disentanglers now have a blocking/truncation role similar to the w tensors. This allows for the optimisation to scale as $\chi_U^4\chi_L^4$. Restricting $\chi_U < \chi_L$ does not seem to greatly decrease the accuracy of the converged MERA (as long as the restriction is not too great), but does allow for much faster runtime. The tensor u now performs a double role, both reducing the entanglement across the boundary of a block as before, and discarding the high energy subspace.

3.2.2 Including a projector

The reduced density matrix ρ_{fp} describes two sites, so is a $\chi^2 \times \chi^2$ matrix (when its upper (lower) indices are fused together). As such, it has χ^2 eigenvalues, describing the probability of measuring any of the basis states. Although this spectrum may take any form, for physical states the eigenvalues tend to decay rapidly, meaning that the probability of measuring the system in the majority of the basis states is negligible.
In the MERA, this can easily be verified by looking at the spectrum of ρ_{fp}. Since these vanishingly small values have a negligible effect on the final state, they may be safely neglected through the inclusion of a projector P [4]. This is be chosen such that $\rho \approx P(\rho)$, projecting into the space formed only from the most

significant basis states. P is made of a pair of isometric tensors v, and is written

$P =$  , (3.3)

where the middle index has dimension $\bar{\chi}$. The tensors are optimised as above, to project onto the most significant eigenspace of ρ_{fp}. The error involved in introducing the projector is easily measured as $\epsilon = 1 - \mathrm{Tr}(P\rho)$, and can thus be controlled. Including the projector modifies the various networks, for example, $A_L(h)$ becomes

$P =$ 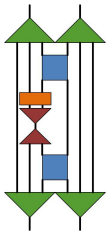 . (3.4)

This network can be contracted in a time proportional to $\chi^6\bar{\chi}$, where $\bar{\chi}$ is the dimension of the dummy index in P. The MERA converges well with $\bar{\chi}$ chosen to be $\mathcal{O}(\chi)$ rather than $\mathcal{O}(\chi^2)$, thus allowing the optimisation algorithm to be computed in time proportional to χ^7 rather than χ^8. Here, it seems that $\bar{\chi} = 5\chi_L$ allows for an accurate algorithm.

3.3 Symmetric MERA

In this section, we will describe how symmetries of the Hamiltonian describing some lattice model can be incorporated into the MERA. This both enforces physical information about the ground state under consideration, and allows for reduction in the required resources. We begin by describing the basic formalism used to describe a subclass of symmetries, using the Ising model as a concrete example.

3.3.1 Symmetries in Quantum Spin Chains

The critical Ising model is described by the Hamiltonian

$$H_{Ising} = \sum_{j=1}^{N} h_{j,j+1} = -\sum_{j=1}^{N} \left(X_j X_{j+1} + Z_j\right). \tag{3.5}$$

This commutes with the symmetry operator

$$S = \prod_{j=1}^{N} Z_j, \tag{3.6}$$

so the model is said to possess a $\mathbb{Z}_2$ symmetry, since S generates a 2^N dimensional representation of the group $\mathbb{Z}_2$. The group $\mathbb{Z}_2$ has two elements e and x such that $e^2 = x^2 = e$ and $ex = xe = x$, exactly the multiplicative properties of S. This is an Abelian group, meaning all elements commute. The discussion here will concern only Abelian groups, although it can be generalised [6,63,64]. In particular, we are interested in on-site symmetries. These are symmetries which can be written as eqn. 3.6; the tensor product of operators on each site, where the set of on-site operators form a matrix representation of the group. Of course, we can use a procedure similar to the preblocking described in eqn. F.1 to redefine what we mean by a site if the 'on-site' operators act on a pair of spins for example.

If we consider a basis for the Hilbert space on a single site, we see that it is spanned by a pair of orthogonal states, $|\uparrow\rangle$ and $|\downarrow\rangle$. Then, $Z|\uparrow\rangle = +|\uparrow\rangle$ and $Z|\downarrow\rangle = -|\downarrow\rangle$. If we then write the matrix Z in the $|\uparrow\rangle$ / $|\downarrow\rangle$ basis (as we usually do), we see it is block diagonal. The representation is decomposed into the direct sum

of the two irreducible representations (irreps) of $\mathbb{Z}_2$. It is a generic feature of symmetric models that the Hilbert space will decompose in this way into sectors which transform according to the different irreps of the symmetry group. For finite Abelian groups, the irreps are all one dimensional, and so are exactly given by the character table [65]. For $\mathbb{Z}_2$, the table is

	e	x
χ_1	1	1
χ_2	1	-1

Table 3.3.1 : The character table for $\mathbb{Z}_2$. Here, e and x label the group elements and χ_1,χ_2 label the two irreps.

Given a state which transforms according to some irrep, we can assign it a conserved charge labelling its irrep. Thus for the Ising model, we can assign the $|\uparrow\rangle$ state a charge '$+$' and the $|\downarrow\rangle$ state a charge '$-$'. If we now take the combined Hilbert space $\mathcal{H}_1 \otimes \mathcal{H}_2$ on a pair of spins, we can then use the product basis $\{|\uparrow\uparrow\rangle, |\uparrow\downarrow\rangle, |\downarrow\uparrow\rangle, |\downarrow\downarrow\rangle\}$. Clearly, the symmetry operator restricted to the pair is $Z_1 Z_2$. Looking at how the product states transform, we see that now

$$Z_1 Z_2 |\uparrow\uparrow\rangle = + |\uparrow\uparrow\rangle \qquad Z_1 Z_2 |\downarrow\downarrow\rangle = + |\downarrow\downarrow\rangle \tag{3.7}$$

$$Z_1 Z_2 |\uparrow\downarrow\rangle = - |\uparrow\downarrow\rangle \qquad Z_1 Z_2 |\downarrow\uparrow\rangle = - |\downarrow\uparrow\rangle . \tag{3.8}$$

This gives us rules for combining the charges, known as *fusion rules*. The fusion rules for $\mathbb{Z}_2$ are $\pm \times \pm = +$, $\pm \times \mp = -$. Choosing a different basis, the *symmetry adapted basis*, we see from eqn. 3.5 that the Hamiltonian on a pair of spins i and $i+1$ is

$$h_{i,i+1} = \begin{array}{c} \\ \langle\uparrow\uparrow| \\ \langle\downarrow\downarrow| \\ \langle\uparrow\downarrow| \\ \langle\downarrow\uparrow| \end{array} \begin{array}{c} \begin{array}{cccc} |\uparrow\uparrow\rangle & |\downarrow\downarrow\rangle & |\uparrow\downarrow\rangle & |\downarrow\uparrow\rangle \end{array} \\ \left(\begin{array}{cc|cc} -1 & -1 & \multicolumn{2}{c}{\multirow{2}{*}{0}} \\ -1 & 1 & & \\ \hline \multicolumn{2}{c|}{\multirow{2}{*}{0}} & -1 & -1 \\ & & -1 & 1 \end{array}\right) \end{array}, \tag{3.9}$$

where the red entries are in the plus sector and the blue entries in the minus sector. There is no coupling between states with different charges, and so the charge is conserved. To enforce the symmetry in the MERA, we simply have to ensure this conservation law is obeyed.

3.3.2 Symmetric tensor networks

Here, we will describe how the conservation law for the charges described above can be incorporated into the MERA network. Symmetries have been previously incorporated into tensor networks in general and the MERA in particular [6–8], however the particular implementation used here is original. It is based on discussions with Guifre Vidal, and a comment in [5]. We will show how this leads to a decrease in required resources.

3.3.3 Symmetric Tensors

The basic unit for the symmetric MERA is the symmetric tensor. This is a tensor which is the direct generalisation of eqn. 3.9, in that it has zeros in the regions which couple different charges. We can decompose each of the indices $i = 1 \ldots \chi$ into their different charges, so they now run over $i = (d, c)$, where $d = 1 \ldots \chi/2$,

and $c = +, -$. As such, a two index tensor M has broken into four sections. Two of these are zero, so we can write

$M =$ 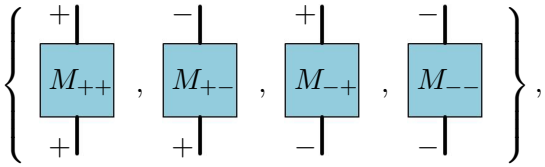

, (3.10)

where each M_{c_1,c_2} corresponds to one of the blocks in eqn. 3.9. We can then generalise this to arbitrary rank tensors simply by ensuring that the product of all the charges is $+$, the trivial charge.

3.3.4 Directed Networks

By assigning a direction of flow, we can think of the network as a circuit with charge preserving gates. We then ensure that the total charge flowing into the bottom of a tensor is the same as the total charge flowing out at the top, as in eqn. 3.11. The direction of an index can be reversed by exchanging the charge for its inverse, the charge $\bar{c}$ such that $c \times \bar{c} = 0$, where 0 is the trivial charge. For the $\mathbb{Z}_2$ symmetry, the inverse of each charge is itself, and so we can ignore the directionality. The condition on the tensors is then that the total ingoing charge equals the total outgoing charge. We can then perform the entire algorithm described above at the level of the blocks in eqn. 3.10, without ever storing or multiplying any elements that are constrained to be zero. The new blocks then carry the charge of the free indices from the contracted blocks

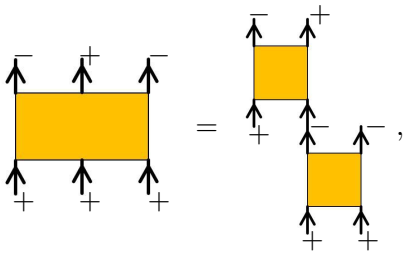
= , (3.11)

The contraction algorithm must check that the intermediate tensor blocks produced along the contraction path all conserve charge, otherwise their existence is forbidden, meaning the entries are all zero so the block is neglected. In this way, the size of the tensors that must be contracted is much smaller, containing only half the number of entries that are present in the full tensors. As such, the algorithm is capable of working in time proportional to χ^8/n, where n is the number of charges in the model (2 for $\mathbb{Z}_2$). In particular, the entire algorithm can be carried out by considering the blocks only, and never reconstructing the full tensors.

3.3.5 Learning how to contract

We wish to have a single algorithm which is capable of performing all the contractions required to execute the optimisation algorithm. Checking the charge conservation condition is satisfied on each iteration is time consuming and unnecessary. Any particular contraction allows some blocks to contract with some other blocks. This pairing of contractable blocks will remain the same for every iteration, so we need only compute the sequence once for every contraction in the MERA. On the first iteration of the MERA, we compute a map associated with each contraction, which is then used on each subsequent iteration to direct the allowed block pairing. This becomes particularly important for the rank six tensors, which have n^6 blocks, but far fewer allowed pairings.

3.4 Resource saving resulting from these modifications

Once these modifications have been added to the basic MERA algorithm described in chapter 2, we obtain a more efficient algorithm. The symmetry constraints provide a multiplicative factor ($1/2$ for the $\mathbb{Z}_2$ symmetry) but do not reduce the scaling of the algorithm with χ. Due to the learning process described above,

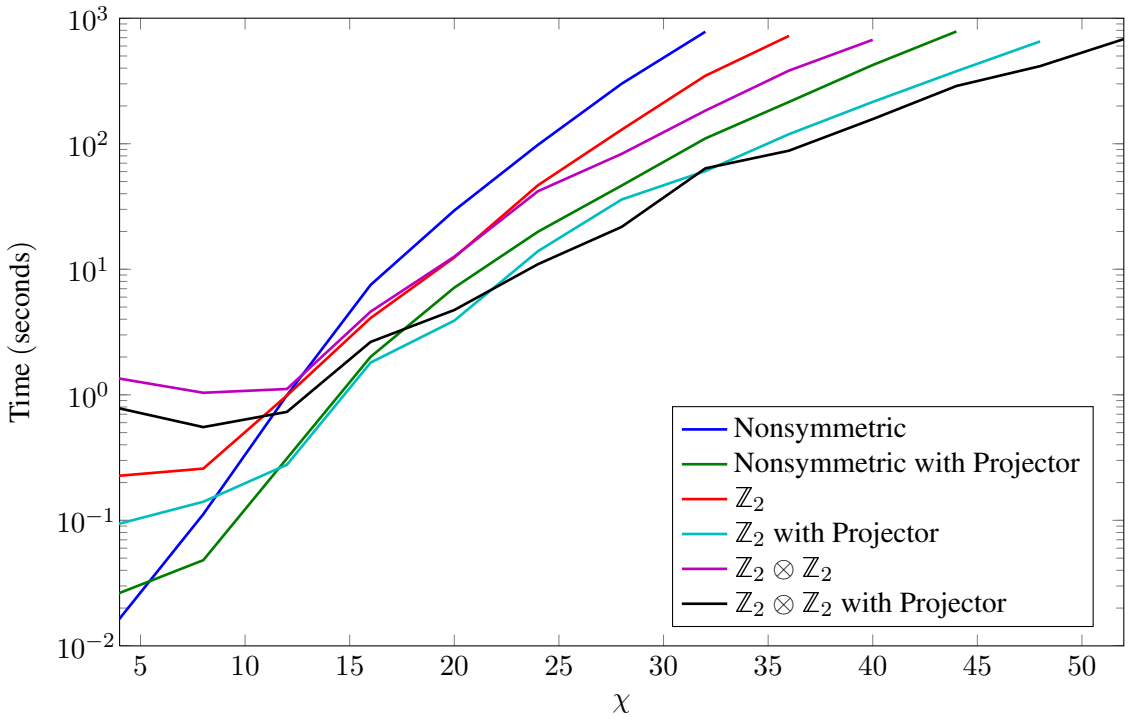

Figure 3.4.1 : Time for one contraction of the descending superoperator with the various modifications to the basic algorithm described here. This benchmarking performed on a machine with 3.46GHz processor. The $\mathbb{Z}_2 \otimes \mathbb{Z}_2$ symmetry will be introduced in the next chapter. Here, $\chi_L = \chi_U = \bar{\chi}/5$. This represents approximately 1/30th of the time to perform one iteration of the optimisation algorithm.

the overhead associated with enforcing the symmetry is negligible. By adding the projector, we can achieve an algorithm which scales as χ^7 rather than χ^8. The time taken for the contraction of the descending superoperator described above is shown in fig. 3.4.1. This represents around $1/30$th of the time to perform one iteration of the optimisation algorithm. More details are included in appendix B.

In this chapter, we have demonstrated several methods which allow for a decrease in computational resources required to optimise the MERA. Preprocessing the tensors allows for faster optimisation and less chance of becoming stuck in local minima. The other two methods involve incorporating physical constraints or properties of the system of interest such that irrelevant values are not calculated and stored.

Chapter 4

Lattice Models with Critical Lines

Over the preceding two chapters, we have described an algorithm which can be used to optimise the multi-scale entanglement renormalisation ansatz to represent the ground state of a critical quantum spin chain. We described how our modifications provide a speed-up in the implementation by making use of the properties of the physical systems. In particular, we showed how the symmetries of the model could be incorporated to gain a multiplicative decrease in required resources. We further showed how, by incorporating a projector, we could decrease the scaling of the algorithm with the bond dimension, allowing for more accurate results.

In this chapter, we will describe a new lattice model, the perturbed cluster model, which we have constructed, and show how its ground state energy and phase structure can be calculated. Further, we will identify a conformal field theory which we predict describes the thermodynamic limit of this model. Both the Ashkin-Teller and perturbed cluster spin chains will be investigated using the MERA algorithm, so we identify symmetries of the Hamiltonians which can be incorporated into the code. These models have a more complex phase structure than the majority of models upon which the MERA has been applied previously. We will examine how the conformal spectrum varies as parameters in the models are changed. Since these models are supposed to be described by different CFTs with continuously varying scaling dimensions, it is interesting to apply the MERA to both.

4.1 Perturbed Cluster Model

Recall from section 1.2.2 that the AT model is described by the Hamiltonian

$$H_{AT} = -\sum_{j=1}^{N} \sigma_j^Z + \tau_j^Z + \lambda \sigma_j^Z \tau_j^Z + \beta \left(\sigma_j^X \sigma_{j+1}^X + \tau_j^X \tau_{j+1}^X + \lambda \sigma_j^X \tau_j^X \sigma_{j+1}^X \tau_{j+1}^X \right), \tag{4.1}$$

which we think of as a pair of Ising chains which have been coupled by a four spin interaction. This model possesses a $\mathbb{Z}_2 \otimes \mathbb{Z}_2$ symmetry associated with spin flips about the Z axis. The group is generated by

$$S_1 = \prod_{j=1}^{N} \sigma_j^Z, \tag{4.2}$$

$$S_2 = \prod_{j=1}^{N} \tau_j^Z. \tag{4.3}$$

This is the type of symmetry which can be incorporated into the MERA; on-site and Abelian. Since there are four elements in the group, incorporating this should provide a fourfold decrease in the computation time after the overheads associated with the enforcement are exceeded.

Using a nonlocal unitary mapping based on that described in [9], we can construct a model which we will refer to as the perturbed cluster model (pCL). The mapping is described in appendix D). This is related to an important model in the field of measurement based quantum computation (MBQC) [10, 66]. MBQC is a scheme for computation which makes use of single qubit measurements only. Performing complex multiqubit gates has proved experimentally challenging [67]. In contrast, single qubit measurements are

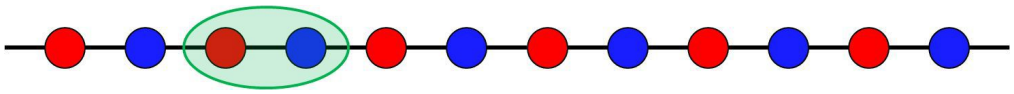

Figure 4.1.1 : We can think of the perturbed cluster model as being defined on a single spin $1/2$ chain. The red operators act only on the red (odd) spins and the blue act only on the blue (even) spins. The green region indicates one site.

much easier to carry out. Since these measurements cannot create entanglement, an entangled resource state is used, the most common is the cluster state [10]. The cluster state is the unique ground state of the cluster Hamiltonian $H_{CL} = -\sum_{j=1}^{N} Z_j X_{j+1} Z_{j+2}$. If such a Hamiltonian described a crystal, a quantum computer would emerge simply by cooling it.

The perturbed cluster model is described by the Hamiltonian

$$\begin{aligned} H_{pCL} = &- \sum_{j=1}^{N} X_j + X_j + \lambda X_j X_j \\ &- \sum_{j=1}^{N-1} \beta \left[Z_j X_j Z_{j+1} + Z_j X_{j+1} Z_{j+1} + \lambda Z_j Y_j Y_{j+1} Z_{j+1} \right]. \end{aligned} \tag{4.4}$$

It is convenient to think of this as a linear chain as shown in fig. 4.1.1. The two colours of the operators in eqn. 4.4 simply distinguish odd numbered spins from the even numbered ones, so X acts on odd spins and X on even ones.

This model represents a cluster Hamiltonian with $\mathbb{Z}_2 \otimes \mathbb{Z}_2$ symmetry respecting perturbations. That is, the terms added to the Hamiltonian all possess the $\mathbb{Z}_2 \otimes \mathbb{Z}_2$ symmetry. This is a particularly important model as its critical line represents the transition from a computational phase, where the model remains a resource for MBQC, to the trivial phase where it cannot be used [67, 68]. Understanding this transition is of key importance to quantum information and computation theory.

Under the mapping used to construct eqn. 4.4, the symmetry remains on-site. The new generators are

$$S_1 = \prod_{j=1}^{N} X_j, \tag{4.5}$$

$$S_2 = \prod_{j=1}^{N} X_j, \tag{4.6}$$

corresponding to flipping all the red (blue) spins about the X axis.

Since these models are unitarily equivalent, they have the same phase structure, shown in fig. 4.1.2. They also have the same ground state energies, as described below. The conformal field theories describing the two models in the continuum limit are not expected to be identical however, since the map is nonlocal and dependent on the boundary conditions as shown in appendix D.

4.2 Ground State Energy

Using a nonlocal unitary transformation, the Ashkin-Teller model can be mapped onto a well understood model known as the XXZ chain [69]. This allows us to calculate the ground state energy per site (GSE) due to a Bethe Ansatz solution [70] for XXZ. The ground state energy for all three models as a function of λ is

$$E_0 = \lambda - 4\sin^2\left(\cos^{-1}(\lambda)\right) \int_0^{\infty} dx \frac{\operatorname{sech}(\pi x)}{\cosh(2\pi \cos^{-1}(\lambda)) - \lambda}. \tag{4.7}$$

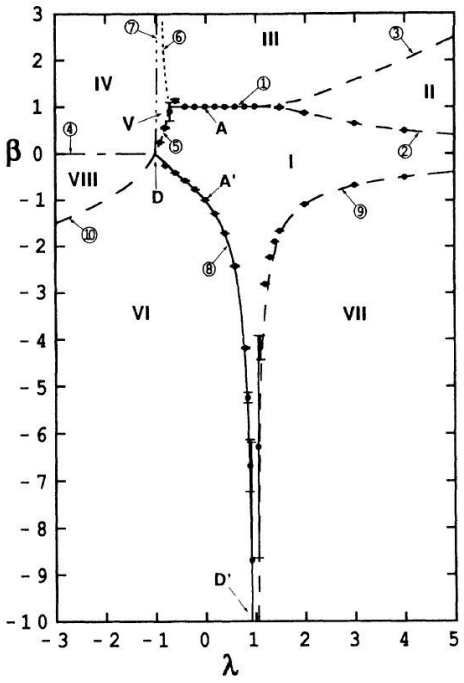

Figure 4.1.2 : The Ashkin-Teller model has a far more complex phase structure than the Ising model. In particular, it has critical lines, rather than points, which allows parameters to vary while the model remains critical. This is of interest for investigation with the MERA algorithm. This figure reproduced from [26].

Since the GSE is an exact property of these lattice models, it provides a good benchmarking quantity. Allowing us to ensure the MERA is a good approximation to the ground state of the Hamiltonian.

4.3 Conformal Field Theories

The thermodynamic limit of a critical lattice model is described by a conformal field theory, as discussed in chapter 1. In particular, the limit of the Ashkin-Teller model is generally accepted to be described by the $S^1/\mathbb{Z}_2$ orbifold boson (obCFT) CFT [33, 35, 71–74]. We would like to note that the model has been historically misidentified with the S^1 boson CFT [73].

Recall from section 1.4 that a CFT can be completely specified by its central charge c, a list of its primary fields ϕ, their associated dimensions Δ_ϕ and spin numbers, and the OPE coefficients describing the result of bringing two fields to the same location. Here we will focus on c and Δ_ϕ.

For the CFT, it is most convenient to parametrise the theory with the compactification radius R, which is related to the AT coupling parameter λ [23] by

$$R_{AT}^2 = \frac{\pi}{2\cos^{-1}(-\lambda)}. \tag{4.8}$$

As the radius is varied, the scaling dimensions are expected to vary continuously as the model is moved along the critical line, due to the presence of an exactly marginal operator [22, 75]. This has fixed scaling dimension 2 for all values of R.

Due to the nonlocal map between AT and pCL, it is not expected that the CFT description should necessarily be the same. In particular, this mapping is highly sensitive to the boundary conditions as shown in appendix D. We can construct a local unitary equivalence between the XXZ and pCL models. As such, we expect the CFTs to be the same for these two models. The thermodynamic description of the XXZ model is the S^1 boson CFT, so we conjecture that this also describes the perturbed cluster model. This CFT also has

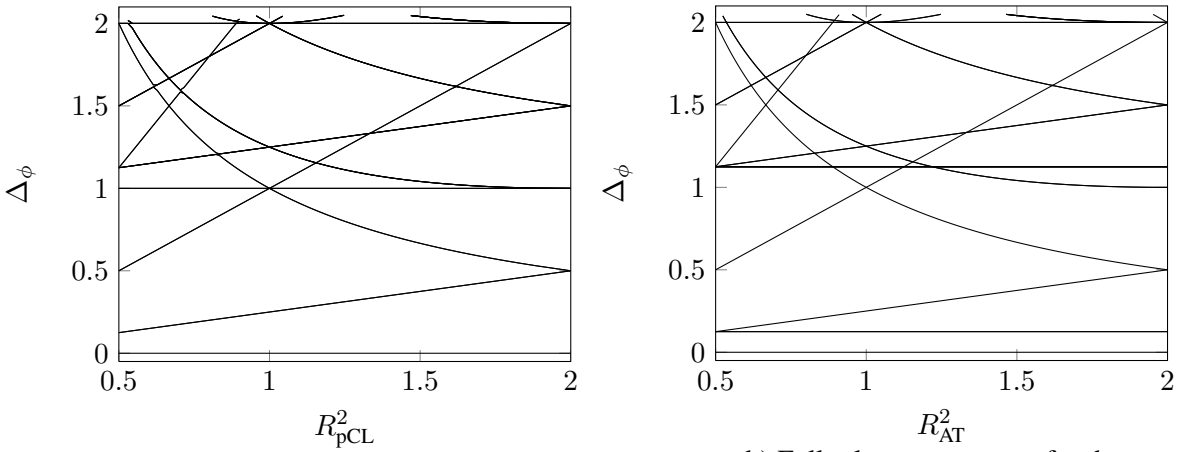

a) Full relevant spectrum for the S^1 boson CFT.

b) Full relevant spectrum for the $S^1/\mathbb{Z}_2$ orbifold boson CFT.

Figure 4.3.1 : Full spectra for the two CFTs as the radii are varied. Notice the presence of the twist fields at constant scaling dimensions $1/8$, $9/8$ and the absence of the fields with dimension 1 in (b).

a compactification radius which may be varied. This is related to the pCL parameter via

$$R^2_{pCL} = \frac{2}{\pi}\left(\pi - \cos^{-1}(\lambda)\right). \tag{4.9}$$

Both the S^1 boson and $S^1/\mathbb{Z}_2$ orbifold boson CFTs have central charge $c = 1$.

The S^1 boson CFT is the field theory of a free massless boson on a circle [33]. The scaling dimensions of the quasivacuum states for this theory are given by

$$\Delta_{e,m} = \frac{e^2}{R^2} + \frac{m^2 R^2}{4}, \tag{4.10}$$

where e and m are two integers labelling the fields. Descendants have scaling dimensions $\Delta_{e,m} + n$, for integer n. More details can be found in [33–35, 37]. The scaling dimensions of the obCFT are the same as the S^1 theory, however the degeneracy is halved since m is restricted to be nonnegative. The obCFT also has a fixed or twisted sector. The scaling dimensions of the fields in this sector do not change as the radius is varied. The S^1 boson lacks this sector, and as such these fields should be absent in the MERA data if the conjecture is correct. The full spectra of these theories is shown in fig. 4.3.1, and more details are included in appendix E.

We have now constructed all the tools necessary to simulate these symmetric critical spin models efficiently. We have described two models of interest, the Ashkin-Teller and perturbed cluster spin chains. Using a unitary map to the XXZ model, we have calculated the ground state energies of the two models. We have also identified CFTs hypothesised to describe the thermodynamic limit of these lattices. In the next chapter, we apply the $\mathbb{Z}_2 \otimes \mathbb{Z}_2$ symmetric MERA to simulating these two chains. We then extract conformal data, and compare it to that of the two CFTs described here.

Chapter 5

$\mathbb{Z}_2 \otimes \mathbb{Z}_2$ Symmetric MERA Examination of the pCL and AT Models

In the preceding chapters, we have described the MERA algorithm, and how it can be adapted to incorporate symmetries in the model under examination. This leads to a decrease in the computational resources required to implement the algorithm. In the last chapter, we described a pair of models; the Ashkin-Teller (AT) and perturbed cluster (pCL) models. Each of these has a $\mathbb{Z}_2 \otimes \mathbb{Z}_2$ on-site symmetry. In this chapter, we will demonstrate how a $\mathbb{Z}_2 \otimes \mathbb{Z}_2$ symmetric MERA can be used to extract physical properties of these models. In particular, we will show how we can recover the ground state energy of these two models as the Hamiltonian parameters are varied, remaining on the critical line at all times. We will then examine the conformal data extracted from the converged MERA, and how this matches the conjectured CFT descriptions. We begin by examining the numerical ground state energy per site. Later, we extract the conformal data as the coupling parameter is varied. In particular, we obtain the central charge, and examine how the scaling dimensions vary as the model is moved along the critical line. The MERA's ability to reproduce the behaviour of models at critical points has been demonstrated [3–5, 60, 61, 76, 77], however the impact of moving along critical lines has not previously been investigated.

5.1 $\mathbb{Z}_2 \otimes \mathbb{Z}_2$ symmetry

The $\mathbb{Z}_2 \otimes \mathbb{Z}_2$ symmetry present in both the AT and pCL models is enforced in the way described in chapter 3. Here, there are four charges, corresponding to the four irreducible representations of $\mathbb{Z}_2 \otimes \mathbb{Z}_2$. We label these $(0,0)$, $(0,1)$, $(1,0)$ and $(1,1)$, and the fusion rules are element-wise addition modulo 2 (i.e. $(1,0) \times (1,1) = (0,1)$).

Each of the scaling operators (eigenoperators of S) can then be assigned a unique charge ¢. The matrix representing it has all zero elements in all charge sectors except that associated with ¢. This allows us to decompose the spectrum into the four charge sectors.

5.2 Ground State Energy

Since we know the ground state energy (GSE) per site exactly, we can use this to check the convergence of our symmetric MERA algorithm. Fig. 5.2.1 shows the ground state energies obtained from the MERA by

$E =$ 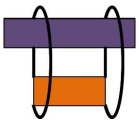 . (5.1)

The relative error in the GSE is given by

$$\Delta E = \frac{E_{\text{exact}} - E_{\text{MERA}}}{E_{\text{exact}}}, \tag{5.2}$$

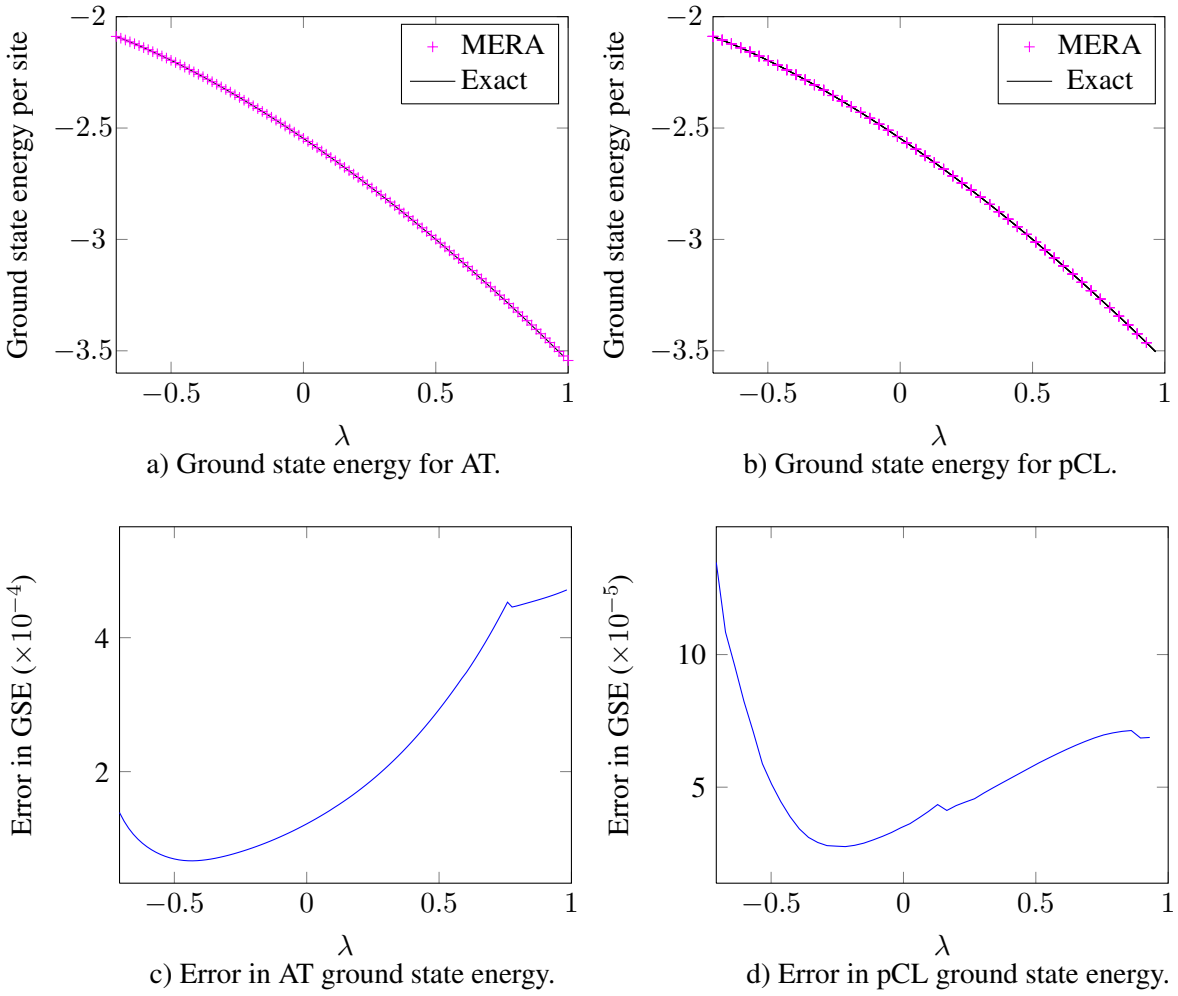

a) Ground state energy for AT.

b) Ground state energy for pCL.

c) Error in AT ground state energy.

d) Error in pCL ground state energy.

Figure 5.2.1 : Ground state energies (GSE) extracted from the MERA. (a) and (c) show the GSE and the error for the Ashkin-Teller model. Here, $\chi_L = 12$, $\chi_U = 8$ and no projector was used. In total, 100 points were converged. (b) and (d) show the GSE and the error for the perturbed cluster model. Here, $\chi_L = \chi_U = 20 = \bar{\chi}/4$. In total, 50 points were converged. The lines marked 'exact' are obtained from numerical integration of eqn. 4.7. We clearly see a decrease in the error at larger χ as expected.

which is clearly only positive if $(E_{\text{exact}} - E_{\text{MERA}}) < 0$. The exact solution is obtained by numerically integrating eqn. 4.7. The MERA in the absence of a projector represents a valid quantum state, and as such, the GSE extracted must be an upper bound on the true GSE. From fig. 5.2.1 (b), we see that this is the case. Fig. 5.2.1 (d) indicates that the presence of a projector, and as such a MERA which is not necessarily an exact quantum state does not significantly degrade the validity of the output; the numerical GSE remains an upper bound at all times.

5.3 Conformal Data

In this section, we will present and comment on the conformal data obtained from the symmetric MERA for the two models under investigation. We will use the parameter R, which is the compactification radius of the conjectured CFT description. Recall, these are related to the coupling parameters by

$$R^2_{AT} = \frac{\pi}{2\cos^{-1}(-\lambda)}, \qquad R^2_{pCL} = \frac{2}{\pi}\left(\pi - \cos^{-1}(\lambda)\right). \tag{5.3}$$

We will examine how the MERA scaling dimensions vary as R is varied, but we begin by investigating the central charge.

5.3.1 Varying R-Stepping method

In the following results, the MERA was initially converged at a single point ($\lambda = -\sqrt{2}/2$). Once this had ceased to vary by more than a threshold value on a given iteration, the optimisation was declared complete. The tensors from this MERA were then used as the initial tensors for the next point and the process was repeated. In this way, the optimisation time could be minimised, since the change in the ground state is assumed to be small between each point.

5.3.2 Central Charge

As discussed above, one of the pieces of data required to specify a CFT is the central charge. This labels classes of CFT and is identically 1 for all values of R in both the S^1 boson and obCFT. The values obtained from the $\mathbb{Z}_2 \otimes \mathbb{Z}_2$ symmetric MERA using eqn. 2.27 are shown in fig. 5.3.1.

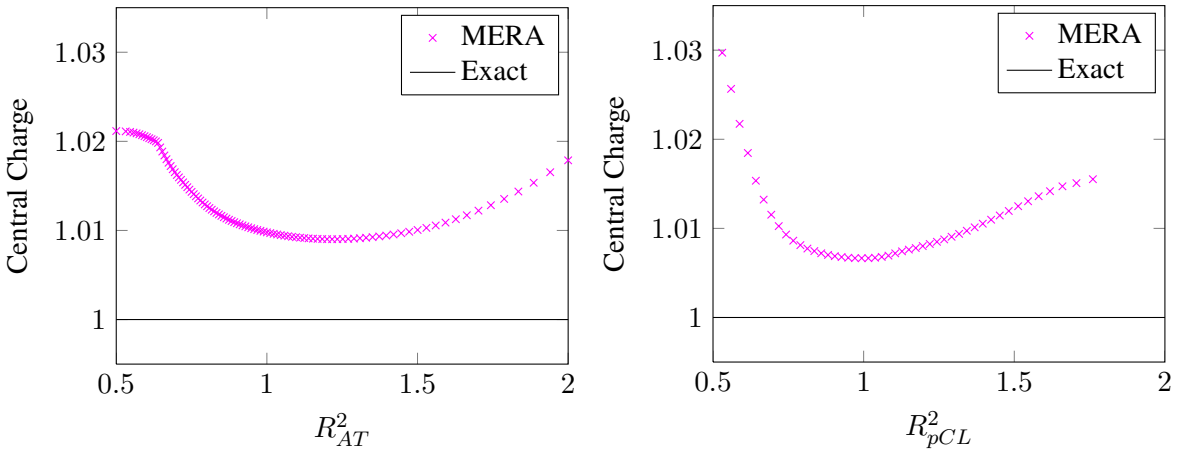

a) Central charge for AT.

b) Central charge for pCL.

Figure 5.3.1 : Central charges extracted from the MERA. (a) shows c for the Ashkin-Teller model. Here, $\chi_L = 12$, $\chi_U = 8$ and no projector was used. In total, 100 points were converged. (b) shows the c for the perturbed cluster model. Here, $\chi_L = \chi_U = 20 = \bar{\chi}/4$. In total, 50 points were converged. The lines marked 'exact' are the expected central charges from the CFTs.

For all values of R, the central charge remains within approximately 3% of the value expected from the CFT. As we move towards the ends of the critical line, we observe the error increase in fig. 5.3.1 (a) and (b), and fig. 5.2.1 (c) and (d). At the ends of the critical lines, new operators become relevant which move the model away from criticality [78]. We conclude that these *marginally irrelevant* fields break scale invariance, thus making the MERA used here, which has imposed scale invariance, invalid. This is consistent with previous MERA simulations, particularly with the Heisenberg model [4]. This spin chain is unitarily equivalent to both Hamiltonians considered here when $\lambda = 1$.

5.3.3 Scaling Dimensions

The central charge obtained from both MERA is consistent with the CFTs of interest, however this is not enough to completely specify the conformal field theory. Thus, we must examine the other conformal data. In particular, we now look at the scaling dimensions from the MERA. We begin by investigating two points along the critical line of the Ashkin-Teller model. In particular, we will present scaling dimensions for the relevant and marginal fields at the decoupling point ($\lambda = 0$, $R^2_{AT} = 1$) where the two Ising chains are uncoupled, and one end of the critical line, which we will refer to as the KT point, where, $\lambda = -\frac{\sqrt{2}}{2}$, $R^2_{AT} = 2$.

5.3.3.1 Ashkin-Teller Decoupling and KT points

Recall from section 1.4 that there are two types of fields present in the CFT, primary fields, and the descendants, which are constructed from the primaries. The associated scaling dimensions for all relevant fields are shown in fig. 5.3.2. This shows the clear signature of the orbifold theory, having both moving and fixed sectors. By this, we mean that the scaling dimensions in the $(0, 0)$ and $(1, 1)$ sectors vary as the coupling parameter is changed, whereas those in the remaining sectors are fixed. We see that the accuracy of the MERA decreases as the scaling dimension increases. This is consistent with the observed behaviour for other models, for example [4, 76, 77]. The number of descendent fields in the CFT is infinite, and due to the finite value of χ, the MERA can only recover a finite subset. Those with smallest scaling dimension are the most accurate, since they are close to the ground state of the theory [61].

We have shown that the MERA provides scaling dimensions for the Ashkin-Teller model which are consistent with the obCFT, which is thought to describe its thermodynamic limit. This has been demonstrated at two values of the coupling In the next section, we show how the MERA captures the behaviour of the CFT as the parameter is varied.

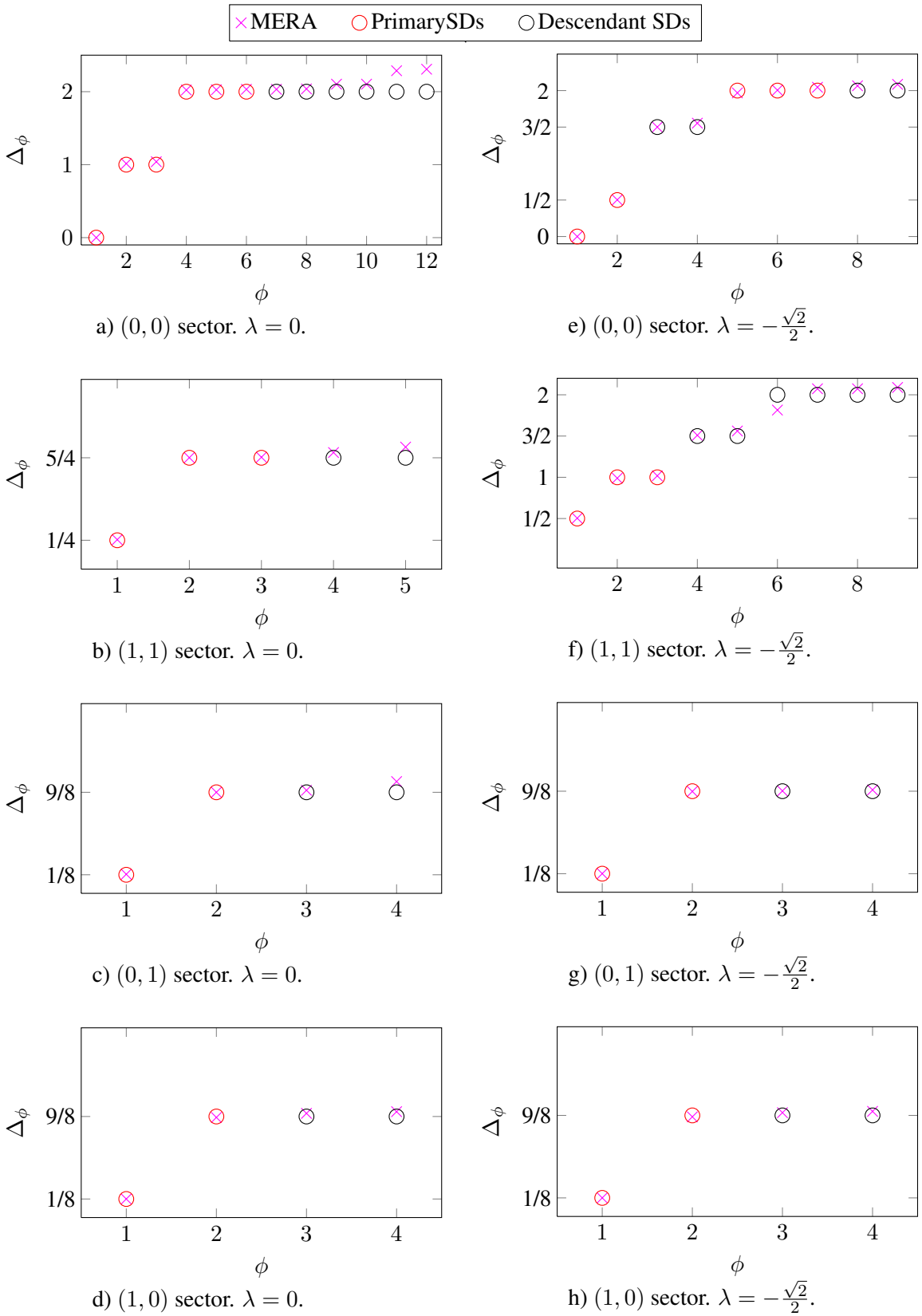

Figure 5.3.2 : Scaling dimensions in the four charge sectors of the Ashkin-Teller model at the decoupling point ($\lambda = 0$) and the KT point ($\lambda = -\frac{\sqrt{2}}{2}$). For (a)-(d), $\chi_L = 28 = \bar{\chi}/5$, $\chi_U = 12$. For (e)-(h), $\chi_L = 36 = \bar{\chi}/4$, $\chi_U = 20$. Open symbols denote obCFT scaling dimensions, with primary fields marked in red, descendants in black. ϕ is an index assigned to the states in each sector.

5.3.4 Continuously Varying Criticality

As the coupling parameter is varied, the scaling dimensions of the two CFTs also change. This is a feature which is not present in CFTs with $c < 1$. This class of models represents the majority of the MERA literature for which conformal data has been published. Investigating the ability of the MERA to replicate this behaviour was one of the main aims of this project, and as such, the current section represents one of the main results of this thesis.

In fig. 5.3.3, we show the data obtained from the MERA in two representative symmetry sectors for both the Ashkin-Teller and perturbed cluster chains. The full result set can be seen in appendix C.

In the $(0,0)$ sector, the two CFTs are identical apart from a doubling of the degeneracy in the S^1 model. The CFTs differ significantly in the $(0,1)$ sector however. The S^1 boson theory does not have a fixed sector, and for the pCL model, we recover the behaviour predicted by the conjectured CFT, providing evidence that this is indeed the correct limiting description.

Due to the extremely large computational investment required to produce this large density of sample points, the values of χ used here are much smaller than those which give the conformal data presented in fig. 5.3.2. As expected, this leads to a less accurate results, particularly for larger scaling dimension.

The region of fig. 5.3.3 (d) (enlarged in fig. 5.3.4) indicated by a box is of particular interest, and we discuss the implications below.

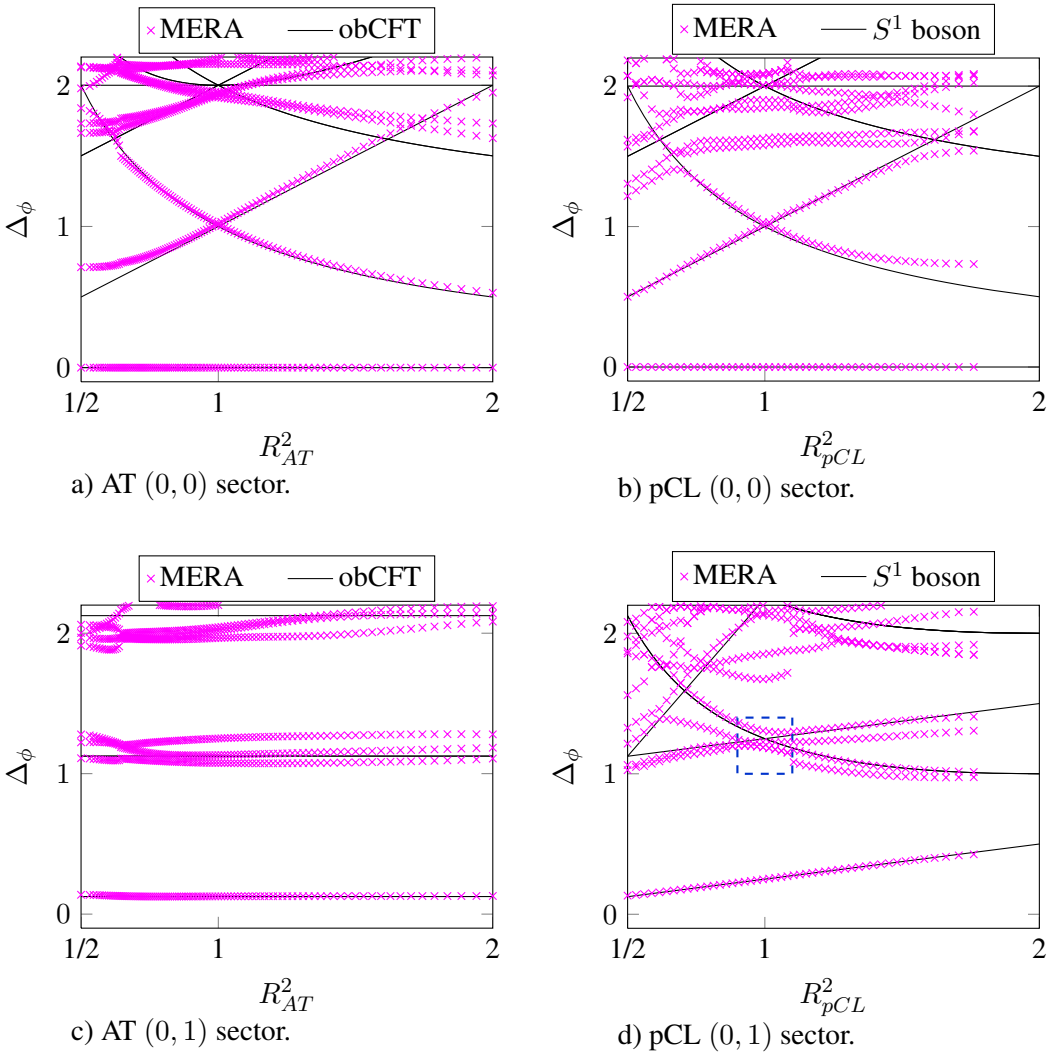

a) AT $(0,0)$ sector.
b) pCL $(0,0)$ sector.
c) AT $(0,1)$ sector.
d) pCL $(0,1)$ sector.

Figure 5.3.3 : Scaling dimensions in two of the four symmetry sectors. (a) and (c) are results for the Ashkin-Teller model. Here, $\chi_L = 12$, $\chi_U = 8$ and no projector was used. In total, 100 points were converged. (b) and (d) show the results in the same sectors for the perturbed cluster model. Here, $\chi_L = \chi_U = 20 = \bar{\chi}/4$. In total, 50 points were converged. Full results can be seen in appendix C. The indicated region is discussed in the main text, and are shown enlarged in fig. 5.3.4.

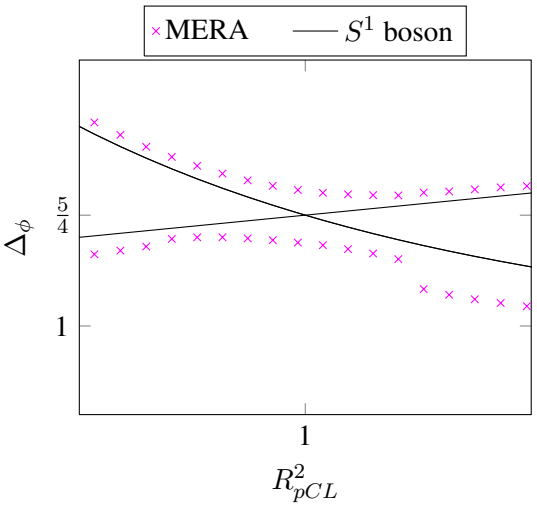

b) pCL $(0, 1)$ sector.

Figure 5.3.4 : Enlargements of the boxed region in fig. 5.3.3 (d). Here, only a subset of the scaling dimensions are shown for clarity. Discussed in the main text.

5.3.4.1 Avoided Crossing at $R^2_{pCL} = 1$

From fig. 5.3.4, we notice an avoided crossing in the MERA output which does not occur in the CFT associated with this model. The states in the CFT with these energies become degenerate at the crossing point. In the CFT, there exists a larger symmetry group, giving a larger set of charges or quantum numbers. The crossing fields do not have a complete set of matching quantum numbers, so cannot mix. The $\mathbb{Z}_2 \otimes \mathbb{Z}_2$ symmetry imposed in the MERA is not the full symmetry group of the models described here. The Ashkin-Teller model has a D_4 symmetry, where the increased symmetry is associated with swapping red and blue. By not imposing the full symmetry of the model, the tensors forming the MERA have nonzero elements which are forbidden in the physical system. This results in coupling between states which should be uncoupled, providing a means for an avoided crossing to occur. This larger symmetry group is non-Abelian, and therefore to enforce this requires significant modifications [63, 64] to the algorithm described in chapter 3. We expect that imposing this would remove the avoided crossing, and speed up computation time. Increasing χ should lead to a better representation of the true ground state of the model, and as such better replication of the behaviour expected from the CFT.

5.4 Insights

From the $\mathbb{Z}_2 \otimes \mathbb{Z}_2$ symmetric MERA used here, we have been able to extract ground state energies as the models are moved along their critical lines. These are consistent with the exact GSE obtained from the Bethe Ansatz solution of the unitarily equivalent XXZ model. At all times, the numerical GSE remains an upper bound on the true energy, in both the MERA without a projector, which produces a true wavefunction, and the modification which incorporates a projector, thus giving only an approximate wavefunction.

The behaviour of the scaling dimensions obtained with the symmetric MERA is consistent with that predicted by the CFTs. We have used this to provide evidence in support of our conjecture that the thermodynamic limit of the perturbed cluster model is described by the S^1 boson conformal field theory.

By investigating the behaviour of the errors in the GSE and central charge, we have seen behaviour consistent with new fields becoming marginal and relevant in the conformal field theories. These marginally irrelevant fields break scale invariance, breaking the assumptions used in the construction of the MERA.

As a result of not enforcing the full symmetry of the models, we observe avoided crossings as operators become degenerate. We expect that incorporating the full, non-Abelian symmetry would prevent this, whilst also providing further computational speed-up.

Chapter 6

Discussion, Conclusions and Future Work

In this thesis, we have developed an algorithm to efficiently optimise the multiscale entanglement renormalisation ansatz to represent the ground state of a large class of critical quantum spin chains. We have incorporated Abelian symmetries present in the Ashkin-Teller and perturbed cluster Hamiltonians, providing a reduction in the computational resources required to implement the algorithm by multiplicative factor. Further, we have incorporated an approximation into the algorithm. This introduces a controlled amount of error into the converged tensor network, and allows for an improvement in the scaling of the algorithm with χ, the parameter controlling the accuracy of the approximation to the ground state. The reduction in the computational requirements of these modified algorithms has also been shown.

This work has examined how the ground state energy and conformal data can be replicated as the Hamiltonian is moved along the critical line. Previous work has looked at critical points or single points on critical lines, so this represents a major advance. We have demonstrated how the MERA can replicate the behaviour expected from the conformal field theory. In particular, we have observed behaviour consistent with the $S^1/\mathbb{Z}_2$ orbifold boson CFT from simulation of the Ashkin-Teller lattice. We also extract scaling dimensions for the perturbed cluster spin chain which are consistent with the continuum limit being described by the S^1 boson conformal field theory.

The results presented here show how avoided crossings can occur if the full symmetry group is not explicitly enforced. In particular, we have imposed the $\mathbb{Z}_2 \otimes \mathbb{Z}_2$ Abelian subgroup of the full D_4 symmetry of the Ashkin-Teller chain. A decrease in the accuracy of the MERA is observed as new fields become relevant in the associated CFT. The effect of these is to move the model away from criticality and break the assumption of scale invariance; a crucial assumption in the ansatz.

We have constructed a model, the perturbed cluster model and used unitary equivalence to an exactly solved model to deduce the ground state energy. We have used the local equivalence to the XXZ model to conjecture the CFT describing the thermodynamic limit of this Hamiltonian. Using our symmetric MERA, we have provided evidence to support this hypothesis.

A clear next step is to optimise a MERA with larger χ to extract more accurate conformal data. This may require a different MERA scheme. The modified binary MERA described in [4] can be optimised with resources that scale as χ^6, potentially allowing far more accurate approximations. Enforcing a larger symmetry group, the computational requirements could be reduced. Both models considered here have and on-site D_4 symmetry. To incorporate this non-Abelian symmetry would require significant modification to the algorithm described here, but would potentially provide more accurate results, for lower computational cost.

Although not described here, it is possible to extract scaling dimensions corresponding to a class of highly nonlocal operators from the MERA at no additional computational expense [77]. Examining the behaviour of these operators as the coupling parameters are varied is currently under way.

It has been suggested that the ability of the MERA to represent the ground state of 1D spin chains is a discrete version of the AdS$_{D+1}$/CFT$_D$ correspondence [44, 79, 80]. Although the MERA has been shown to reproduce the scaling dimensions of the conformal field theory, no method has been described which allows extraction of the 'spin' number [35]. The spin quantum number in the CFT is associated with rotational invariance of spacetime, a property which has no clear analogy in the MERA. Extraction of the spin number is possible using other numerical techniques, such as exact diagonalisation [81]. The recovery of this data

from the MERA remains an open question, however if the MERA truly represents a discretised anti-de Sitter space, it would appear that this should be possible.

In conclusion, this work represents the first attempt to apply the MERA to models with complex phase structures, and to recover the behaviour of the model as the scale invariant ground state is varied.

References

[1] G. Vidal, "Entanglement Renormalization", Physical Review Letters **99**, 220405 (2007).

[2] G. Evenbly and G. Vidal, "Algorithms for entanglement renormalization", Physical Review B **79**, 144108 (2009).

[3] G. Evenbly, *Foundations and Applications of Entanglement Renormalization*, PhD Thesis, The University of Queensland, 2010.

[4] G. Evenbly and G. Vidal, "Quantum Criticality with the Multi-scale Entanglement Renormalization Ansatz", (2011), arXiv:1109.5334v1 [quant-ph].

[5] R. N. C. Pfeifer, *Simulation of Anyons Using Symmetric Tensor Network Algorithms*, PhD Thesis, The University of Queensland, 2011.

[6] S. Singh, R. Pfeifer, and G. Vidal, "Tensor network decompositions in the presence of a global symmetry", Physical Review A **82**, 050301 (2010).

[7] S. Singh, R. Pfeifer, and G. Vidal, "Tensor network states and algorithms in the presence of a global U(1) symmetry", Physical Review B **83**, 115125 (2011).

[8] B. Bauer, P. Corboz, R. Orús, and M. Troyer, "Implementing global Abelian symmetries in projected entangled-pair state algorithms", Physical Review B **83**, 125106 (2011).

[9] A. Doherty and S. Bartlett, "Identifying Phases of Quantum Many-Body Systems That Are Universal for Quantum Computation", Physical Review Letters **103**, 020506 (2009).

[10] R. Raussendorf and H. J. Briegel, "A One-Way Quantum Computer", Physical Review Letters **86**, 5188–5191 (2001).

[11] M. A. Nielsen and I. L. Chuang, *Quantum computation and quantum information* (Cambridge University Press, Cambridge; New York, 2000).

[12] A. Kay and D. G. Angelakis, "Reproducing spin lattice models in strongly coupled atom-cavity systems", Europhysics Letters **84**, 20001 (2008).

[13] F. Verstraete, V. Murg, and J. Cirac, "Matrix product states, projected entangled pair states, and variational renormalization group methods for quantum spin systems", Advances in Physics **57**, 143–224 (2008).

[14] D. V. Dmitriev, V. Y. Krivnov, A. A. Ovchinnikov, and A. Langari, "One-dimensional anisotropic Heisenberg model in the transverse magnetic field", Journal of Experimental and Theoretical Physics **95**, 538–549 (2002).

[15] P. W. Anderson *et al.*, "The physics behind high-temperature superconducting cuprates: the plain vanilla version of RVB", Journal of Physics: Condensed Matter **16**, R755–R769 (2004).

[16] S. Sachdev, "Tensor networks: a new tool for old problems", Physics **2**, 90 (2009).

[17] M. Oshikawa, "Fractionalization and Topological Order", in *Understanding quantum phase transitions*, edited by L. Carr, chap. 4, 91–113, CRC Press, Boca Raton, 2011.

[18] A. Dutta *et al.*, "Transverse field spin models: From Statistical Physics to Quantum Information", (2010), arXiv:1012.0653v1 [cond-mat.stat-mech].

[19] S. Sachdev, *Quantum phase transitions*, 2nd ed. (Cambridge University Press, Cambridge, 2011).

[20] J. Ashkin and E. Teller, "Statistics of two-dimensional lattices with four components", Physical Review **64**, 178–184 (1943).

[21] J. Sólyom, "Duality of the block transformation and decimation for quantum spin systems", Physical Review B **24**, 230–243 (1981).

[22] L. P. Kadanoff and A. C. Brown, "Correlation functions on the critical lines of the Baxter and Ashkin-Teller models", Annals of Physics **121**, 318–342 (1979).

[23] M. Kohmoto, M. den Nijs, and L. Kadanoff, "Hamiltonian studies of the d= 2 Ashkin-Teller model", Physical Review B **24**, 5229–5241 (1981).

[24] F. Igloi and J. Solyom, "Phase diagram and critical properties of the (1+1)-dimensional Ashkin-Teller model", Journal of Physics A: Mathematical and General **17**, 1531–1545 (1984).

[25] G. von Gehlen and V. Rittenberg, "The Ashkin-Teller quantum chain and conformal invariance", Journal of Physics A: Mathematical and Theoretical **20**, 227–237 (1987).

[26] M. Yamanaka, Y. Hatsugai, and M. Kohmoto, "Phase diagram of the Ashkin-Teller quantum spin chain", Physical Review B **50**, 559–562 (1994).

[27] P. Bak, P. Kleban, W. Unertl, and J. Ochab, "Phase diagram of selenium adsorbed on the Ni (100) surface: A physical realization of the Ashkin-Teller model", Physical Review Letters **54**, 1539–1542 (1985).

[28] V. Aji and C. M. Varma, "Theory of the Quantum Critical Fluctuations in Cuprate Superconductors", Physical Review Letters **99**, 067003 (2007).

[29] C. Gils, "Ashkin-Teller universality in a quantum double model of Ising anyons", Journal of Statistical Mechanics: Theory and Experiment **2009**, P07019 (2009).

[30] P. Calabrese and J. Cardy, "Entanglement entropy and quantum field theory", Journal of Statistical Mechanics: Theory and Experiment **2004**, P06002 (2004).

[31] J. Eisert, "Colloquium: Area laws for the entanglement entropy", Reviews of Modern Physics **82**, 277–306 (2010).

[32] G. Vidal, J. I. Latorre, E. Rico, and A. Kitaev, "Entanglement in Quantum Critical Phenomena", Physical Review Letters **90**, 227904 (2003).

[33] P. Di Francesco, *Conformal field theory* (Springer, New York, 1997).

[34] R. Blumenhagen, *Introduction to conformal field theory : with applications to string theory* (Springer, Berlin; New York, 2009).

[35] P. Ginsparg, "Applied Conformal Field Theory", (1988), arXiv:9108028.

[36] J. Cardy, "Boundary Conformal Field Theory", (2004), arXiv:0411189.

[37] J. G. Polchinski, *String theory, An Introduction to the Bosonic String* (Cambridge University Press, Cambridge, UK; New York, 1998).

[38] K. Wilson, "The renormalization group: Critical phenomena and the Kondo problem", Reviews of Modern Physics **47**, 773–840 (1975).

[39] N. Goldenfeld, *Lectures on phase transitions and the renormalization group* (Addison-Wesley, Reading, 1992).

[40] M. Fisher, "Renormalization group theory: Its basis and formulation in statistical physics", Reviews of Modern Physics **70**, 653–681 (1998).

[41] G. Evenbly and G. Vidal, "Entanglement renormalization in free bosonic systems: real-space versus momentum-space renormalization group transforms", New Journal of Physics **12**, 025007 (2010).

[42] A. Tsvelik, *Quantum field theory in condensed matter physics* (Cambridge University Press, Cambridge, UK, 2003).

[43] D. Amit and V. Martin-Mayor, *Field Theory; The Renormalization Group and Critical Phenomena*, 3rd ed. (World Scientific Publishing Company, Singapore, 2005).

[44] G. Evenbly and G. Vidal, "Tensor Network States and Geometry", Journal of Statistical Physics **145**, 891–918 (2011).

[45] J. D. Biamonte, S. R. Clark, and D. Jaksch, "Categorical Tensor Network States", AIP Advances **1**, 042172 (2011).

[46] D. Perez-Garcia, F. Verstraete, M. M. Wolf, and J. I. Cirac, "Matrix product state representations", Quantum Information and Computation **7**, 401–430 (2007).

[47] F. Verstraete and J. I. Cirac, "Renormalization algorithms for Quantum-Many Body Systems in two and higher dimensions", (2004), arXiv:0407066.

[48] Y.-Y. Shi, L.-M. Duan, and G. Vidal, "Classical simulation of quantum many-body systems with a tree tensor network", Physical Review A **74**, 022320 (2006).

[49] A. Y. Bogdanov, Y. I. Bogdanov, and K. A. Valiev, "Schmidt modes and entanglement in continuous-variable quantum systems", Russian Microelectronics **35**, 7–20 (2006).

[50] G. H. Liu, W. Li, and W. L. You, "Bipartite entanglement of the one-dimensional extended quantum compass model in a transverse field", The European Physical Journal B **85**, 1–6 (2012).

[51] F. Verstraete and J. Cirac, "Matrix product states represent ground states faithfully", Physical Review B **73**, 094423 (2006).

[52] M. B. Hastings, "An area law for one-dimensional quantum systems", Journal of Statistical Mechanics: Theory and Experiment **2007**, P08024–P08024 (2007).

[53] A. Daley, C. Kollath, U. Schollwöck, and G. Vidal, "Time-dependent density-matrix renormalization-group using adaptive effective Hilbert spaces", Journal of Statistical Mechanics: Theory and Experiment **2004**, P04005 (2004).

[54] G. Vidal, "Efficient Classical Simulation of Slightly Entangled Quantum Computations", Physical Review Letters **91**, 147902 (2003).

[55] F. Verstraete, J. J. García-Ripoll, and J. I. Cirac, "Matrix Product Density Operators: Simulation of Finite-Temperature and Dissipative Systems", Physical Review Letters **93**, 207204 (2004).

[56] C. Menotti, C. Trefzger, and M. Lewenstein, "Metastable States of a Gas of Dipolar Bosons in a 2D Optical Lattice", Physical Review Letters **98**, 235301 (2007).

[57] B. Pirvu, G. Vidal, F. Verstraete, and L. Tagliacozzo, "Matrix product states for critical spin chains: Finite-size versus finite-entanglement scaling", Physical Review B **86**, 075117 (2012).

[58] F. Pollmann, S. Mukerjee, A. Turner, and J. Moore, "Theory of Finite-Entanglement Scaling at One-Dimensional Quantum Critical Points", Physical Review Letters **102**, 255701 (2009).

[59] R. A. Horn and C. R. Johnson, *Topics in matrix analysis* (Cambridge University Press, Cambridge; New York, 1991).

[60] V. Giovannetti, S. Montangero, and R. Fazio, "Quantum Multiscale Entanglement Renormalization Ansatz Channels", Physical Review Letters **101**, 180503 (2008).

[61] R. Pfeifer, G. Evenbly, and G. Vidal, "Entanglement renormalization, scale invariance, and quantum criticality", Physical Review A **79**, 040301 (2009).

[62] G. Vidal, "Private communications".

[63] S. Singh, R. Pfeifer, and G. Vidal, "Tensor network states and algorithms in the presence of a global SU (2) symmetry", (2012), arXiv:1208.3919 [cond-mat.str-el].

[64] S. Singh, *Tensor Network States and Algorithms in the presence of Abelian and non-Abelian Symmetries*, PhD Thesis, The University of Queensland, 2012, arXiv:1203.2222v2.

[65] P. Ramond, *Group theory : a physicist's survey* (Cambridge University Press, Cambridge, UK; New York, 2010).

[66] M. Nielsen, "Cluster-state quantum computation", Reports on Mathematical Physics **57**, 147–161 (2006).

[67] D. V. Else, I. Schwarz, S. D. Bartlett, and A. C. Doherty, "Symmetry-Protected Phases for Measurement-Based Quantum Computation", Physical Review Letters **108**, 240505 (2012).

[68] D. V. Else, S. D. Bartlett, and A. C. Doherty, "Symmetry protection of measurement-based quantum computation in ground states", (2012), arXiv:1207.4805v2 [quant-ph].

[69] C. C. Rulli and M. S. Sarandy, "Entanglement and local extremes at an infinite-order quantum phase transition", Physical Review A **81**, 032334 (2010).

[70] F. C. Alcaraz, M. N. Barber, and M. T. Batchelor, "Conformal invariance, the XXZ chain and the operator content of two-dimensional critical systems", Annals of Physics **182**, 280–343 (1988).

[71] M. Yamanaka and M. Kohmoto, "Line of continuously varying criticality in the Ashkin-Teller quantum chain", Physical Review B **52**, 1138–1143 (1995).

[72] S. Yang and H. Zheng, "Superconformal invariance in the two-dimensional Ashkin-Teller model", Nuclear Physics B **285**, 410–422 (1987).

[73] S. Yang, "Modular invariant partition function of the Ashkin-Teller model on the critical line and N= 2 superconformal invariance", Nuclear Physics B **285**, 183–203 (1987).

[74] H. Saleur, "Partition functions of the two-dimensional Ashkin-Teller model on the critical line", Journal of Physics A: Mathematical and General **20**, L1127–L1133 (1987).

[75] L. P. Kadanoff and F. J. Wegner, "Some critical properties of the eight-vertex model", Physical Review B **4**, 3989–3993 (1971).

[76] G. Vidal, "Entanglement Renormalization: An Introduction", in *Understanding quantum phase transitions*, edited by L. Carr, chap. 5, 115–138, CRC Press, Boca Raton, 2011.

[77] G. Evenbly, P. Corboz, and G. Vidal, "Nonlocal scaling operators with entanglement renormalization", Physical Review B **82**, 132411 (2010).

[78] S. Eggert, "Numerical evidence for multiplicative logarithmic corrections from marginal operators", Physical Review B **54**, R9612–R9615 (1996).

[79] B. Swingle, "Entanglement renormalization and holography", Physical Review D **86**, 065007 (2012).

[80] J. Molina-Vilaplana and P. Sodano, "Holographic view on quantum correlations and mutual information between disjoint blocks of a quantum critical system", Journal of High Energy Physics **2011** (2011).

[81] R. N. C. Pfeifer, "Classification of topological symmetry sectors on anyon rings", Physical Review B **85**, 245126 (2012).

[82] W. Son, L. Amico, and V. Vedral, "Topological order in 1D Cluster state protected by symmetry", Quantum Information Processing , 1–8 (2011).

Appendix A

A detailed explanation of the algorithm

In this appendix, we will present a detailed overview of a particular subroutine, so the code in appendix F can be understood.

We number tensors right to left top to bottom, so a generic 6 index tensor is labelled

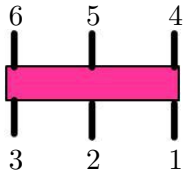

A.1 Contract

The workhorse routine for the MERA is the 'Contract' algorithm. The full code can be seen in section F.2. For the symmetric codes, this is too complicated to describe line by line, so we describe its general purpose and structure.

The routine takes as input a pair of tensors A and B, and vectors $Aindices$, $Bindices$ containing the indices which are to be contracted. Thus, if the first entry of $Aindices$=3 and the first entry of $Bindices$=2, then the third index of A will be contracted with the second index of B. The input $path$ contains a list of the blocks in the symmetric tensors A and B which may be contracted. On the first run, this is empty and the routine explicitly checks charge conservation. After this, so long as the ordering of the blocks in storage is the same, the allowed block pairs remains the same. The routine outputs the result of the contraction C and the vector of blocks $path$ if this was previously empty.

```
1 function [C,path]=Contract(A,B,Aindices,Bindices,path)
```

We use the MATLAB language to implement the MERA as it has highly optimised matrix manipulation libraries. To take advantage of this, we convert all tensors and tensor operations to an equivalent matrix and matrix operation. This is the primary role of the Contract subroutine. A contraction follows the following structure:

- Convert tensors to matrices by permuting then fusing.
- Compute matrix product.
- Convert the matrices back to tensors by unfusing then permuting.

Suppose we wish to contract the third index of one tensor with the second of another, with diagram

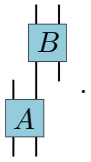

First, we rearrange the indices to place all noncontracted indices on the outside. This can be done with MATLAB's 'permute' function. The result is then

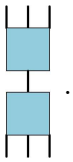

We now fuse the outer indices into a single index. This uses MATLAB's 'reshape' command. This gives a new index $i = i_1 \times i_2$. If we are contracting over more than one index, these are also fused. We then obtain a pair of matrices.

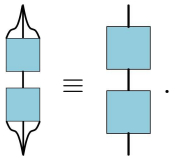

This can then be multiplied using the highly optimised and parallelised MATLAB routine. We must then return the matrix to its tensor form by unfusing the indices.

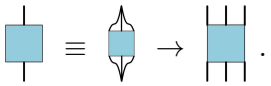

We have now obtained a tensor C which is the contracted version of the start diagram. The ordering of the indices in C is first all the uncontracted indices from A in order followed by those from B in order.

The symmetric tensors are stored in arrays of blocks. For example, a four index $\mathbb{Z}_2$ symmetric tensor is stored as

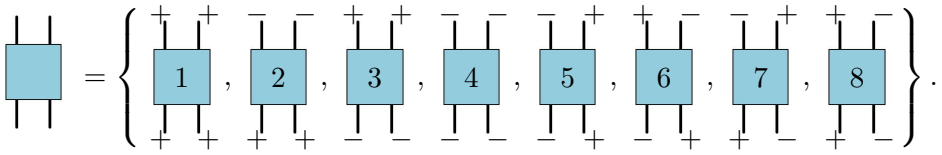

In the case of the above contraction, path would then be

$$\begin{pmatrix} 1 & 1 \\ 1 & 2 \\ 1 & 7 \\ 1 & 8 \\ 2 & 3 \\ 2 & 4 \\ 2 & 5 \\ 2 & 6 \\ 3 & 1 \\ \vdots & \end{pmatrix}$$

where the first column labels blocks in A and the second blocks in B and only the first 9 pairs are shown.

A.2 ASuperoperatorL

We will now describe line by line how a particular subroutine functions. We will use one part of the ascending superoperator as a representative example. This routine is one of 3 required to ascend the Hamiltonian by one layer. Here, we present the routine without a projector for simplicity.

The challenge is to contract the network in an optimal way. Particular choices of contraction order lead to different time and memory costs. We will describe the subroutine line by line. This subroutine is required to contract fig. A.2.1.

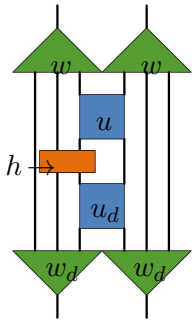

Figure A.2.1 : The left ascending superoperator

Here, we describe the routine line by line.

```
3 persistent path1 path2 path3 path4 path5 path6
```

This line generates empty vectors if they do not already exist. These are used to ensure the correct blocks contract with the correct blocks without having to check. During the first time this routine is run, these vectors are filled with instructions, requiring the Contract routine to check the charges on each leg; an expensive process. On successive runs, this vector is nonempty, and allows the contraction to proceed without any charge checking, greatly speeding up the process, whilst allowing the Contract routine to remain general.

```
5 [temp1,path1]=Contract(w_d,w,4,3,path1);
```

If the vector path1 exists, this is used for the contraction, otherwise it proceeds with checking the associated charges. This line contracts the fourth index of $w^\dagger$ with the third index of w (indicated in red).

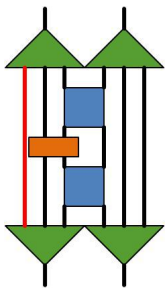

After this contraction has been performed, the new network is

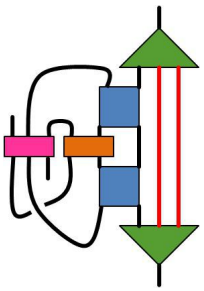

The contraction then continues with the legs indicated in red.

```
6  [temp2,path2]=Contract(w_d,w,[2,3],[1,2],path2);
```

This gives the network

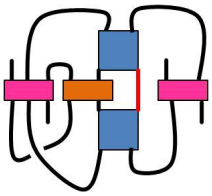

We now contract $u^\dagger$ with u.

```
7  [temp3,path3]=Contract(u_d,u,3,1,path3);
```

The resulting diagram is

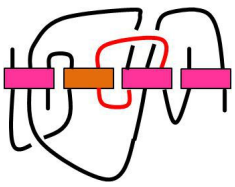

The remaining lines continue in this way, sequentially making the diagram more compact.

```
9  [temp4,path4]=Contract(temp3,o,[3,4],[1,3],path4);
10 [temp5,path5]=Contract(temp1,temp4,[2,3,4,5],[2,5,4,6],path5);
11 [temp6,path6]=Contract(temp5,temp2,[3,4],[2,3],path6);
```

With the diagrammatic version being

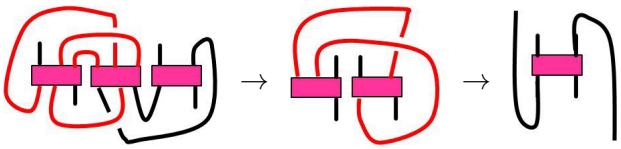

This is not a Hamiltonian, since the indices are in the wrong order. The last two lines bring the indices and their associated charges into the correct order, and the MERA optimisation can continue.

```
A(1,:)=cellfun(@(x)permute(x,[3,1,4,2]),temp6(1,:),'UniformOutput',0);
A(2,:)=cellfun(@(x)x(:,[3,1,4,2]),temp6(2,:),'UniformOutput',0);
```

We finally obtain the ascended Hamiltonian

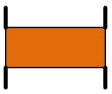

The largest tensor formed in this routine has 6 indices, so the memory scaling will be χ^6. The time scaling can be calculated by counting indices. The number of indices included in a given contraction is the power of χ for that contraction. That is, the total number of indices possessed by the two tensors involved, with the shared legs only being counted once. Here, we see this is 8. Thus this routine has time scaling χ^8, which is optimal for the ternary MERA used here.

The entire code for this routine is below.

```
function A=ASuperoperatorL(u,u_d,w,w_d,o)

persistent path1 path2 path3 path4 path5 path6

[temp1,path1]=Contract(w_d,w,4,3,path1);
[temp2,path2]=Contract(w_d,w,[2,3],[1,2],path2);
[temp3,path3]=Contract(u_d,u,3,1,path3);

[temp4,path4]=Contract(temp3,o,[3,4],[1,3],path4);
[temp5,path5]=Contract(temp1,temp4,[2,3,4,5],[2,5,4,6],path5);
[temp6,path6]=Contract(temp5,temp2,[3,4],[2,3],path6);

A(1,:)=cellfun(@(x)permute(x,[3,1,4,2]),temp6(1,:),'UniformOutput',0);
A(2,:)=cellfun(@(x)x(:,[3,1,4,2]),temp6(2,:),'UniformOutput',0);
```

Appendix B

Scaling of Algorithms with χ

We have fitted a power law of the form $a\chi^b$ to the time taken for the various algorithms to perform one contraction of the descending superoperator. Each point in fig. B.0.1 is averaged over five contractions to reduce noise from background processes. The fit parameters are shown in table B.0.1.

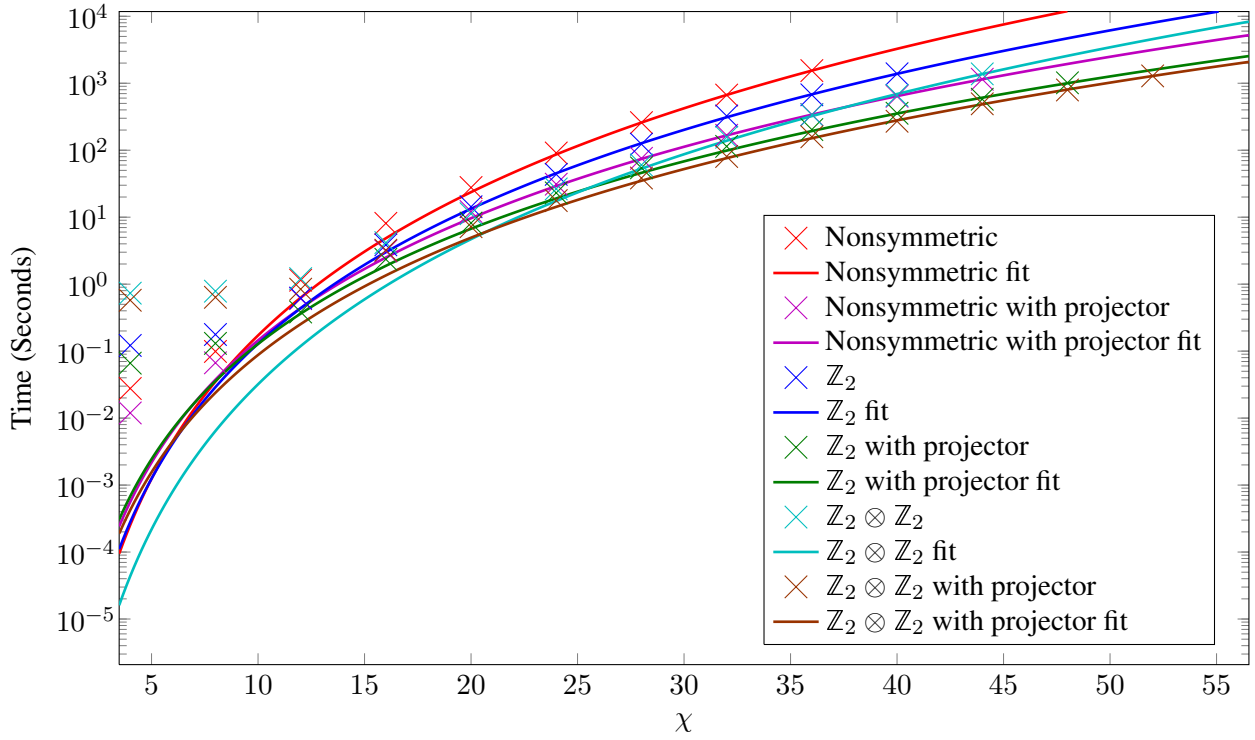

Figure B.0.1 : Time for one contraction of the descending superoperator with the various modifications to the basic algorithm described here. Here, $\chi_L = \chi_U = 1/5\bar{\chi}$. This represents approximately 1/30th of the time to perform one iteration of the optimisation algorithm. Each point is averaged over the time taken for 5 contractions to reduce noise from background processes. This benchmarking performed on a machine with 3.46GHz processor. The fit parameters are shown in table B.0.1.

Algorithm	a	b
Nonsymmetric	1.336×10^{-8}	7.108
Nonsymmetric with projector	1.267×10^{-7}	6.058
$\mathbb{Z}_2$	2.617×10^{-8}	6.693
$\mathbb{Z}_2$ with projector	2.467×10^{-7}	5.715
$\mathbb{Z}_2 \otimes \mathbb{Z}_2$	2.029×10^{-9}	7.189
$\mathbb{Z}_2 \otimes \mathbb{Z}_2$ with projector	1.334×10^{-7}	5.817

Table B.0.1 : Fit parameters for the time to contract the descending superoperator once. Fitted to power law of the form $a\chi^b$

As expected, adding the symmetry does not have a large impact on the scaling of the algorithm. Adding the projector reduces the power b by approximately 1 as designed. Overall, the scaling appears to be one power better than expected. We attibute this to the highly optimised matrix operations present in MATLAB. These improve the naive scaling assumed in the body of this thesis.

Appendix C

Full Conformal Data for the Ashkin-Teller and Perturbed Cluster Models

In this appendix we present the full set of relevant scaling dimensions in all four charge sectors of the Ashkin-Teller and perturbed cluster models. See chapter 5 for analysis.

C.1 Ashkin-Teller

Here, the MERA was converged at the KT point ($\lambda = -\frac{\sqrt{2}}{2}$), then stepped out from here as described in sec. 5.3.1. Recall that

$$R^2_{AT} = \frac{\pi}{2\cos^{-1}(-\lambda)}, \tag{C.1}$$

so the initial convergence was at R^2_{AT}=1.

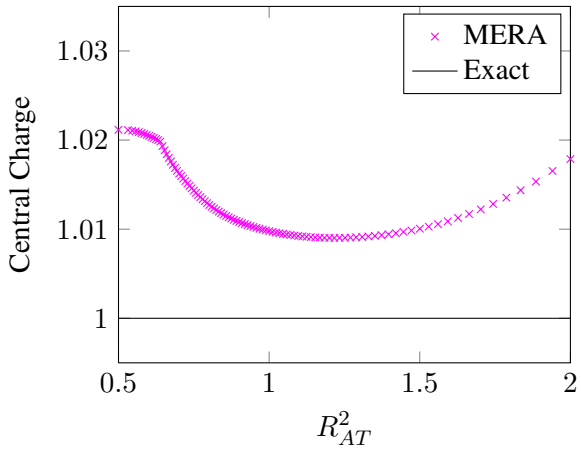

a) Central charge for AT.

Figure C.1.1 : Central charge extracted from the MERA for the Ashkin-Teller model. Here, $\chi_L = 12$, $\chi_U = 8$ and no projector was used. In total, 100 points were converged. The line marked 'exact' are the expected central charge from the obCFT. 5.

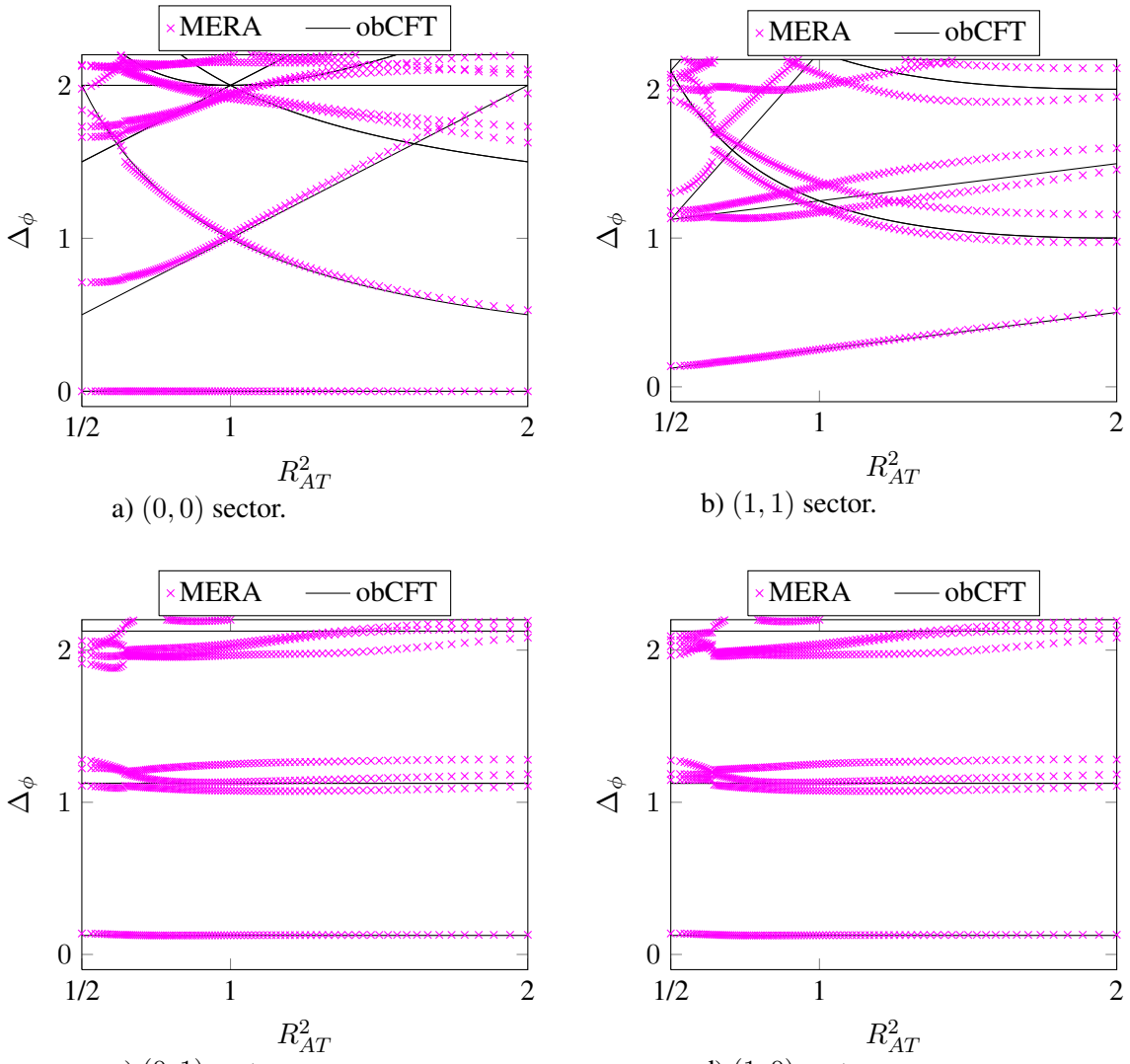

a) $(0,0)$ sector. b) $(1,1)$ sector.

c) $(0,1)$ sector. d) $(1,0)$ sector.

Figure C.1.2 : Scaling dimensions in the four charge sectors of the Ashkin-Teller model. Here, $\chi_L = 12$, $\chi_U = 8$ and no projector was used. In total, 100 points were converged. The boxed region is discussed in chapter 5. (a) and (c) are shown in the main text.

C.2 Perturbed Cluster

Here, the MERA was converged at the KT point ($\lambda = -\sqrt{2}/2$), then stepped out from here as described in sec. 5.3.1. Recall that

$$R^2_{pCL} = \frac{2}{\pi}\left(\pi - \cos^{-1}(\lambda)\right), \tag{C.2}$$

so the initial MERA was at $R^2_{pCL} = 0.5$.

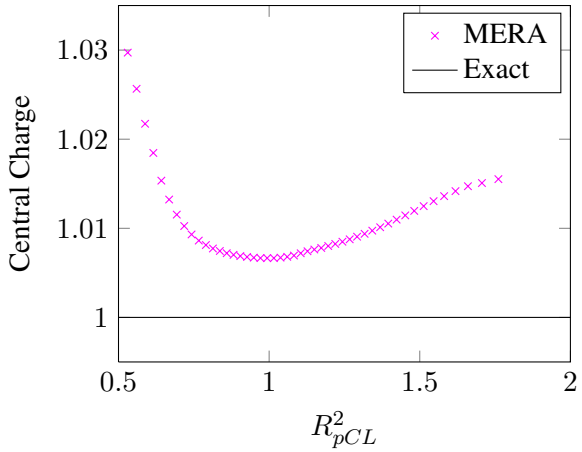

b) Central charge for pCL.

Figure C.2.1 : Central charge extracted from the MERA for the perturbed cluster model. Here, $\chi_L = \chi_U = 20 = \bar{\chi}/4$. In total, 50 points were converged. The line marked 'exact' are the expected central charges from the S^1 boson CFT. Repeated from chapter 5.

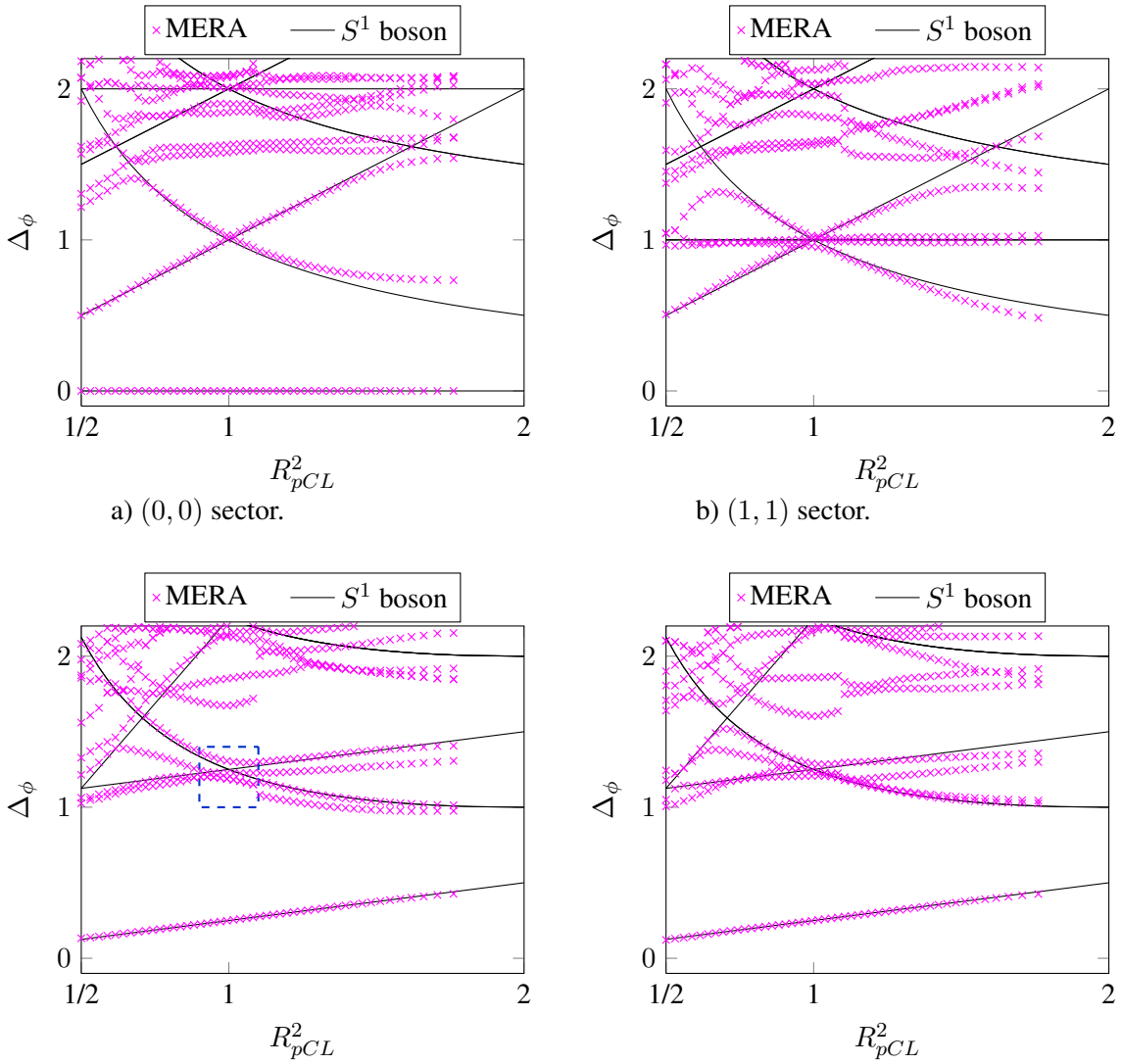

a) $(0,0)$ sector. b) $(1,1)$ sector.

c) $(0,1)$ sector. d) $(1,0)$ sector.

Figure C.2.2 : Scaling dimensions in the four charge sectors of the perturbed cluster model. Here, $\chi_L = \chi_U = 20 = \bar{\chi}/4$. In total, 50 points were converged. The boxed region is discussed in chapter 5. (a) and (c) are shown in the main text.

Appendix D

Duality Mappings

In this appendix, we show how the perturbed cluster model is dual to the Ashkin-Teller model. We will investigate how this mapping is dependent on the boundary conditions and how the symmetries map across. Finally, we will construct the map linking both AT and pCL to the XXZ model. We will show how the equivalence between pCL and XXZ is local and insensitive to boundaries.

D.1 Ashkin-Teller to perturbed cluster

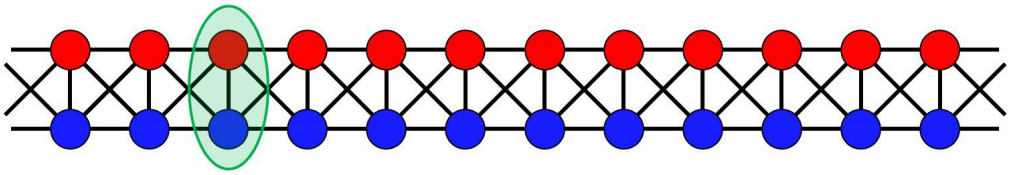

Figure D.1.1 : We can think of the Ashkin-Teller model as being defined on a pair of parallel chains. The σ operators act only on the red chain and the τ act only on the blue. The lines represent coupling present in the Hamiltonian. The green region indicates one site.

The Hamiltonian describing the Ashkin-Teller model (AT) on the chain in fig. D.1.1 is:

$$H = -\sum_{j=1}^{N} \sigma_j^Z + \tau_j^Z + \lambda \sigma_j^Z \tau_j^Z + \beta \left(\sigma_j^X \sigma_{j+1}^X + \tau_j^X \tau_{j+1}^X + \lambda \sigma_j^X \tau_j^X \sigma_{j+1}^X \tau_{j+1}^X \right) \tag{D.1}$$

where $\{\sigma^X, \sigma^Y, \sigma^Z\}$, $\{\tau^X, \tau^Y, \tau^Z\}$ are two sets of mutually commuting Pauli operators, that is they obey the usual Pauli relations within a set and

$$[\sigma_j^{X,Y,Z}, \tau_k^{X,Y,Z}] = 0, \tag{D.2}$$

for all j, k. A site is indicated by the green region in fig. D.1.1.

By generalising a mapping proposed in [9], we obtain a map

$$\begin{aligned} \sigma_j^Z &\to X_j & \tau_j^Z &\to X_j \\ \sigma_j^X &\to \left(\prod_{k=1}^{j} X_k \right) Z_j & \tau_j^X &\to Z_j \left(\prod_{k=j}^{N} X_k \right) \end{aligned} \tag{D.3}$$

With the end spins transforming as above, where the products are not included if the upper limit is smaller than the lower, i.e.

$$\sigma_1^X \to Z_1 \qquad \tau_N^X \to Z_N. \tag{D.4}$$

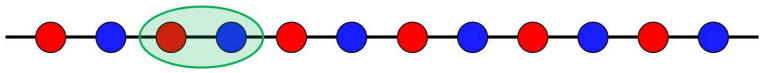

Figure D.1.2 : The chain on which the perturbed cluster model (pCL) is defined

So the Hamiltonian transforms to:

$$\begin{aligned}\bar{H} = &-\sum_{j=1}^{N} X_j + X_j + \lambda X_j X_j - \sum_{j=1}^{N-1} \beta \left[(\prod_{k=1}^{j-1} X_k) Z_j (\prod_{k=1}^{j} X_k) Z_{j+1} \right. \\ &+ Z_j (\prod_{k=j+1}^{N} X_k) Z_{j+1} (\prod_{k=j+2}^{N} X_k) \\ &\left. + \lambda \left((\prod_{k=1}^{j-1} X_k) Z_j Z_j (\prod_{k=j+1}^{N} X_k) (\prod_{k=1}^{j} X_k) Z_{j+1} Z_{j+1} (\prod_{k=j+2}^{N} X_k) \right) \right] \qquad \text{(D.5)} \\ = &-\sum_{j=1}^{N} X_j + X_j + \lambda X_j X_j - \sum_{j=1}^{N-1} \beta \left[Z_j X_j Z_{j+1} + Z_j X_{j+1} Z_{j+1} + \lambda Z_j Y_j Y_{j+1} Z_{j+1} \right]. \qquad \text{(D.6)}\end{aligned}$$

This is the cluster Hamiltonian with 1,2 and 4 spin symmetry respecting perturbations. Defined on the chain in fig. D.1.2. The cluster model (on a line) is defined as the ground state of the cluster Hamiltonian

$$H_{CL} = -\sum_{j=1}^{N-1} Z_j X_j Z_{j+1} + Z_j X_{j+1} Z_{j+1}. \qquad \text{(D.7)}$$

It has been shown that while this state is not a universal resource for measurement based quantum computation (MBQC), any single qubit unitary gate can be performed with perfect fidelity over arbitrary chain lengths [66]. Moreover, there exists a phase defined by the symmetry of the model, such that for symmetry respecting perturbations, a phase transition must be crossed to reach the product state. Within this phase, the identity gate is protected [67]. The perturbed cluster model lies on the boundary of this phase.

For convenience, we give the reverse mapping

$$\begin{aligned} X_j &\to \sigma_j^Z & X_j &\to \tau_j^Z \\ Z_j &\to \left(\prod_{k=1}^{j-1} \tau_k^Z \right) \sigma_j^X & Z_j &\to \tau_j^X \left(\prod_{k=j+1}^{N} \sigma_k^Z \right) \end{aligned} \qquad \text{(D.8)}$$

D.1.1 Generating Set for 2 Site Operators

We now consider how symmetry respecting and breaking perturbations map between the models. A generating set for up to 2 site (4 spin) perturbations, is given by:

$$X_j I_j I_{j+1} I_{j+1} \qquad Z_j I_j I_{j+1} I_{j+1} \qquad \text{(D.9)}$$
$$I_j X_j I_{j+1} I_{j+1} \qquad I_j Z_j I_{j+1} I_{j+1} \qquad \text{(D.10)}$$
$$I_j I_j X_{j+1} I_{j+1} \qquad I_j I_j Z_{j+1} I_{j+1} \qquad \text{(D.11)}$$
$$I_j I_j I_{j+1} X_{j+1} \qquad I_j I_j I_{j+1} Z_{j+1} \qquad \text{(D.12)}$$

Allowing sums and products of these enables construction of any 2 site operator. Then these map to:

$$\sigma_j^Z I_j I_{j+1} I_{j+1} \qquad \left(\prod_{k=1}^{j-1} \tau_k^Z\right) \sigma_j^X \tag{D.13}$$

$$I_j \tau_j^Z I_{j+1} I_{j+1} \qquad \tau_j^X \left(\prod_{k=j+1}^{N} \sigma_k^Z\right) \tag{D.14}$$

$$I_j I_j \sigma_{j+1}^Z I_{j+1} \qquad \left(\prod_{k=1}^{j} \tau_k^Z\right) \sigma_{j+1}^X \tag{D.15}$$

$$I_j I_j I_{j+1} \tau_{j+1}^Z \qquad \tau_{j+1}^X \left(\prod_{k=j+2}^{N} \sigma_k^Z\right) \tag{D.16}$$

Clearly the Y pCL operators map to highly nonlocal operators in AT.

D.1.2 Generating Set for Symmetry Respecting 2 Site Operators

The symmetry respecting 2 site operators are those which commute with representations of $\mathbb{Z}_2 \otimes \mathbb{Z}_2 = D_2$, that is those 4 spin operators commuting with both $X_j X_{j+1}$ and $X_j X_{j+1}$. A generating set for these operators is:

$$X_j I_j I_{j+1} I_{j+1} \qquad Z_j X_j Z_{j+1} I_{j+1} \tag{D.17}$$

$$I_j X_j I_{j+1} I_{j+1} \qquad I_j Z_j X_{j+1} Z_{j+1} \tag{D.18}$$

$$I_j I_j X_{j+1} I_{j+1} \tag{D.19}$$

$$I_j I_j I_{j+1} X_{j+1} \tag{D.20}$$

These then map to:

$$\sigma_j^Z I_j I_{j+1} I_{j+1} \qquad \sigma_j^X \sigma_{j+1}^X \tag{D.21}$$

$$I_j \tau_j^Z I_{j+1} I_{j+1} \qquad \tau_j^X \tau_{j+1}^X \tag{D.22}$$

$$I_j I_j \sigma_{j+1}^Z I_{j+1} \tag{D.23}$$

$$I_j I_j I_{j+1} \tau_{j+1}^Z \tag{D.24}$$

These are all 2 site symmetry respecting operators under the AT symmetry operators $\sigma_j^Z \sigma_{j+1}^Z$ and $\tau_j^Z \tau_{j+1}^Z$, which define the symmetry in the AT model. Thus, all symmetry respecting operators acting on 2 sites in the Ashkin-Teller model map to symmetry respecting operators acting on 2 sites on the perturbed cluster chain. The products of the stabilisers (and their images) are:

$$\left(\prod_{j=1}^{N-1} Z_j X_j Z_{j+1}\right) = Z_1 \left(\prod_{j=1}^{N-1} X_j\right) Z_N \to \sigma_1^X \sigma_N^X \tag{D.25}$$

$$\left(\prod_{j=1}^{N-1} Z_j X_{j+1} Z_{j+1}\right) = Z_1 \left(\prod_{j=2}^{N} X_j\right) Z_N \to \tau_1^X \tau_N^X \tag{D.26}$$

D.2 Boundaries for Even Chains

We now consider how the boundary terms map. We begin by considering a chain with an even number of spins. Let the pCL chain be even length as in fig. D.2.1, that is it begins with a red spin and terminates with a blue spin. Then at the edges, there are 4 operators (2 anticommuting pairs) commuting with all the

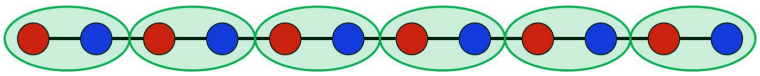

Figure D.2.1 : A pCL chain with an even number of spins.

stabilisers, thus defining 2 qubits (i.e. 2 logical X operators and 2 logical Z operators). These operators (and their AT images) are:

$$X_1 Z_1 \to \left(\prod_{k=1}^{N} \sigma_k^Z\right) \tau_1^X \tag{D.27}$$

$$Z_N X_N \to \sigma_N^X \left(\prod_{k=1}^{N} \tau_k^Z\right) \tag{D.28}$$

$$Z_1 \to \sigma_1^X \tag{D.29}$$

$$Z_N \to \tau_N^X \tag{D.30}$$

These map to non-local operators in AT. Local boundary terms in AT and their images are:

$$\sigma_1^Z \tau_1^X \sigma_2^Z \to X_1 Z_1 \left(\prod_{k=3}^{N} X_k\right) \tag{D.31}$$

$$\tau_{N-1}^Z \sigma_N^X \tau_N^Z \to \left(\prod_{k=1}^{N-2} X_k\right) Z_N X_N \tag{D.32}$$

$$\sigma_1^X \to Z_1 \tag{D.33}$$

$$\tau_N^X \to Z_N \tag{D.34}$$

All the 2 site, symmetry respecting operators defined above map in the same way on the edges.

D.3 Odd length chain

Adding a red spin to the right hand edge of the chain clearly does not change the mapping of the bulk operators. The symmetry respecting edge operators map as above for the generators containing a single X. The cluster stabiliser which has a Z on the additional red spin maps as

$$Z_{N-1} X_{N-1} Z_N \to \sigma_{N-1}^X \sigma_N^X \tag{D.35}$$

as above. Here N is the half filled site containing the added red spin. The other operators acting on the end map as

$$Z_{N-1} X_N \to \tau_{N-1}^X \sigma_N^Z \tag{D.36}$$

$$Z_N \to \left(\prod_{k=1}^{N-1} \tau_k^Z\right) \sigma_N^X. \tag{D.37}$$

If a blue spin is added to the left end of the chain, then

$$X_1 Z_2 \to \sigma_2^X \tag{D.38}$$

$$Z_1 X_2 Z_2 \to \tau_1^X \tau_2^X \tag{D.39}$$

$$Z_1 \to \tau_1^X \left(\prod_{k=2}^{N} \sigma_k^Z\right). \tag{D.40}$$

Adding a blue spin to the left and a red spin to the right is described by these transformations.

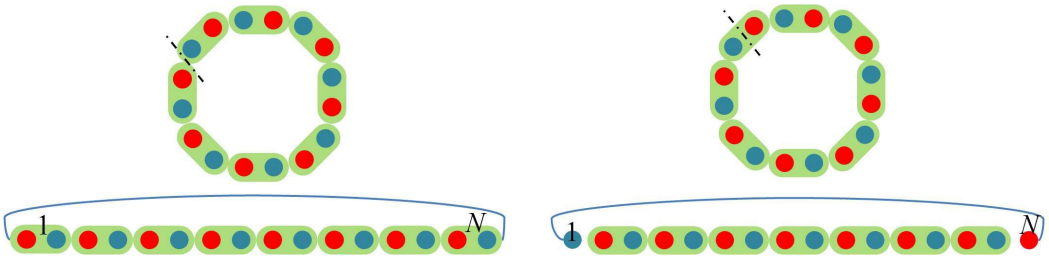

(a) Intersite splitting (b) Intrasite splitting

Figure D.4.1 : Ways to define sites 1 and N on even length periodic chains. Despite having the same number of spins, chain (a) has $N = 8$, whereas (b) has $N = 9$.

D.4 Periodic Boundary Conditions

Given a system with periodic boundary conditions, the 'first site' can be chosen in one of 2 ways, as shown in fig. D.4.1. For the chain in fig. D.1(a), the perturbed cluster Hamiltonian is

$$\begin{aligned} H = &- \beta \left[Z_N X_N Z_1 + Z_N X_1 Z_1 + \lambda Z_N Y_N Y_1 Z_1 \right] - \sum_{j=1}^{N} X_j + X_j + \lambda X_j X_j \\ &- \sum_{j=1}^{N-1} \beta \left[Z_j X_j Z_{j+1} + Z_j X_{j+1} Z_{j+1} + \lambda Z_j Y_j Y_{j+1} Z_{j+1} \right]. \end{aligned} \tag{D.41}$$

Using the mappings above, this becomes

$$\begin{aligned} H = &- \beta \left[\sigma_1^X \sigma_N^X \left(\prod_{k=1}^{N} \tau_k^Z \right) + \left(\prod_{k=1}^{N} \sigma_k^Z \right) \tau_1^X \tau_N^X + \lambda \sigma_1^Y \tau_1^Y \left(\prod_{k=2}^{N-1} \sigma_k^Z \tau_k^Z \right) \sigma_N^Y \tau_N^Y \right] \\ &- \sum_{j=1}^{N} \sigma_j^Z + \tau_j^Z + \lambda \sigma_j^Z \tau_j^Z - \sum_{j=1}^{N-1} \beta \left[\sigma_j^X \sigma_{j+1}^X + \tau_j^X \tau_{j+1}^X + \lambda \sigma_j^X \tau_j^X \sigma_{j+1}^X \tau_{j+1}^X \right]. \end{aligned} \tag{D.42}$$

If this contains highly nonlocal terms due to the boundary. If the AT Hamiltonian were defined on the periodic lattice, it would be

$$\begin{aligned} H = &- \beta \left(\sigma_N^X \sigma_1^X + \tau_N^X \tau_1^X + \lambda \sigma_N^X \tau_N^X \sigma_1^X \tau_1^X \right) - \sum_{j=1}^{N} \sigma_j^Z + \tau_j^Z + \lambda \sigma_j^Z \tau_j^Z \\ &- \sum_{j=1}^{N-1} \beta \left(\sigma_j^X \sigma_{j+1}^X + \tau_j^X \tau_{j+1}^X + \lambda \sigma_j^X \tau_j^X \sigma_{j+1}^X \tau_{j+1}^X \right). \end{aligned} \tag{D.43}$$

Which would map to

$$\begin{aligned} H = &- \beta \left[\left(\prod_{j=1}^{N-1} Z_j X_j Z_{j+1} \right) + \left(\prod_{j=1}^{N-1} Z_j X_{j+1} Z_{j+1} \right) + \lambda \left(\prod_{j=1}^{N-1} Z_j X_j Z_{j+1} Z_j X_{j+1} Z_{j+1} \right) \right] \\ &- \sum_{j=1}^{N} X_j + X_j + \lambda X_j X_j - \sum_{j=1}^{N-1} \beta \left[Z_j X_j Z_{j+1} + Z_j X_{j+1} Z_{j+1} + \lambda Z_j Y_j Y_{j+1} Z_{j+1} \right]. \end{aligned} \tag{D.44}$$

$$
\begin{aligned}
&= -\beta\left[\left(\prod_{j=1}^{N-1} Z_jX_jZ_{j+1}\right)+\left(\prod_{j=1}^{N-1} Z_jX_{j+1}Z_{j+1}\right)+\lambda\left(\prod_{j=1}^{N-1} Z_jY_jY_{j+1}Z_{j+1}\right)\right] \\
&\quad -\sum_{j=1}^{N} X_j + X_j + \lambda X_jX_j - \sum_{j=1}^{N-1}\beta\left[Z_jX_jZ_{j+1}+Z_jX_{j+1}Z_{j+1}+\lambda Z_jY_jY_{j+1}Z_{j+1}\right].
\end{aligned}
\tag{D.45}
$$

$$
\begin{aligned}
&= -\beta\left[\prod_{j=1}^{N-1}\left(Z_jX_jZ_{j+1}+Z_jX_{j+1}Z_{j+1}+\lambda Z_jY_jY_{j+1}Z_{j+1}\right)\right] \\
&\quad -\sum_{j=1}^{N} X_j + X_j + \lambda X_jX_j - \sum_{j=1}^{N-1}\beta\left[Z_jX_jZ_{j+1}+Z_jX_{j+1}Z_{j+1}+\lambda Z_jY_jY_{j+1}Z_{j+1}\right].
\end{aligned}
\tag{D.46}
$$

D.5 Degeneracy with open and periodic boundaries

Considering the bare models with open boundary conditions, that is:

$$
H_{AT,bare} = \sum_{j=1}^{N-1} \sigma_j^X\sigma_{j+1}^X + \tau_j^X\tau_{j+1}^X \tag{D.47}
$$

$$
H_{Cl,bare} = \sum_{j=1}^{N-1} Z_jX_jZ_{j+1} + Z_jX_{j+1}Z_{j+1} \tag{D.48}
$$

It is well know that the cluster Hamiltonian with open boundaries has 4 degenerate ground states due to the removal of 2 of the stabiliser terms [82]. The Ashkin-Teller also clearly has 4 degenerate ground states

$$
|g_1\rangle = |+\rangle|+\rangle \tag{D.49}
$$

$$
|g_2\rangle = |+\rangle|-\rangle \tag{D.50}
$$

$$
|g_3\rangle = |-\rangle|+\rangle \tag{D.51}
$$

$$
|g_4\rangle = |-\rangle|-\rangle \tag{D.52}
$$

where

$$
|+\rangle = |+\rangle_1 \otimes |+\rangle_2 \cdots |+\rangle_N, \tag{D.53}
$$

and so on. In the case where the boundaries are periodic, the degeneracy of the cluster model is broken, however the degeneracy of the Ashkin-Teller model remains as above. In this case, what happens to the mapping?

$$
H_{Cl,bare} = Z_NX_NZ_1 + Z_NX_1Z_1 + \sum_{j=1}^{N-1} Z_jX_jZ_{j+1} + Z_jX_{j+1}Z_{j+1} \tag{D.54}
$$

is the periodic bare cluster Hamiltonian. This maps to

$$
H_{AT,bare} = \sigma_1^X\sigma_N^X\left(\prod_{k=1}^{N}\tau_k^Z\right) + \left(\prod_{k=1}^{N}\sigma_k^Z\right)\tau_1^X\tau_N^X + \sum_{j=1}^{N-1}\sigma_j^X\sigma_{j+1}^X + \tau_j^X\tau_{j+1}^X \tag{D.55}
$$

$$
= \sigma_1^X\sigma_N^X S_{AT,1}^N + S_{AT,1}^N\tau_1^X\tau_N^X + \sum_{j=1}^{N-1}\sigma_j^X\sigma_{j+1}^X + \tau_j^X\tau_{j+1}^X \tag{D.56}
$$

where $S^N_{AT,1}, S^N_{AT,1}$ are τ^Z, σ^Z applied to sites 1 to N. That is, the symmetry operators. This breaks the degeneracy of the model by this string operator. The Hamiltonian is the periodic Ashkin-Teller with these string operators applied. The periodic bare Ashkin-Teller

$$H_{AT,bare} = \sigma^X_N \sigma^X_1 + \tau^X_N \tau^X_1 + \sum_{j=1}^{N-1} \sigma^X_j \sigma^X_{j+1} + \tau^X_j \tau^X_{j+1}, \tag{D.57}$$

maps to

$$H_{Cl,bare} = Z_1 \left(\prod_{k=1}^{N-1} X_k \right) Z_N + Z_1 \left(\prod_{k=2}^{N} X_k \right) Z_N + \sum_{j=1}^{N-1} Z_j X_j Z_{j+1} + Z_j X_{j+1} Z_{j+1} \tag{D.58}$$

The boundary terms can be viewed in 2 ways:

$$Z_1 \left(\prod_{k=1}^{N-1} X_k \right) Z_N = \prod_{j=1}^{N-1} Z_j X_j Z_{j+1} \tag{D.59}$$

$$= Z_N X_N Z_1 \left(\prod_{k=1}^{N} X_k \right) = Z_N X_N Z_1 S^N_{Cl,1} \tag{D.60}$$

$$Z_1 \left(\prod_{k=2}^{N} X_k \right) Z_N = \prod_{j=1}^{N-1} Z_j X_{j+1} Z_{j+1} \tag{D.61}$$

$$= Z_N X_1 Z_1 \left(\prod_{k=1}^{N} X_k \right) = Z_N X_1 Z_1 S^N_{Cl,1} \tag{D.62}$$

where again, $S^N_{Cl,1}$ and $S^N_{Cl,1}$ are the symmetry string operators. The first equality for each of these shows why this maps to a degenerate cluster Hamiltonian. It is mapped to a product of bulk stabilisers, thus is essentially the model with open boundaries. The second equalities show the link to the periodic cluster model, with a string symmetry operator reinstating the degeneracy.

We have shown the mapping between the Ashkin-Teller and perturbed cluster models. We have seen how the symmetries map, and how boundary conditions affect the equivalence. Finally, we have shown how the ground state degeneracy is linked to strings of symmetry operators. We now present the mappings to the XXZ model, and show how for the pCL, this is local and insensitive to boundary conditions.

D.5.1 Ashkin-Teller to XXZ

We can define a mapping from H_{AT} to H_{XXZ} [70]

$$\sigma^Z_j \to \bar{X}_j \bar{X}_j \qquad \tau^Z_j \to \bar{Y}_j \bar{Y}_j \tag{D.63}$$

$$\sigma^X_j \sigma^X_{j+1} \to \bar{Y}_j \bar{Y}_{j+1} \qquad \tau^X_j \tau^X_{j+1} \to \bar{X}_j \bar{X}_{j+1}. \tag{D.64}$$

Then, we obtain

$$H_{XXZ} = -\sum_{j=1}^{N} \bar{X}_j \bar{X}_j + \bar{Y}_j \bar{Y}_j - \lambda \bar{Z}_j \bar{Z}_j - \sum_{j=1}^{N-1} \beta \left[\bar{Y}_j \bar{Y}_{j+1} + \bar{X}_j \bar{X}_{j+1} - \lambda \bar{Z}_j \bar{Z}_{j+1} \right]. \tag{D.65}$$

D.5.2 Perturbed Cluster to XXZ

By combining the above mappings, we obtain a local map between the pCL and XXZ models. Defining the mapping

$$X_j \to \bar{X}_j \bar{X}_j \qquad X_j \to \bar{Y}_j \bar{Y}_j \tag{D.66}$$

$$Z_j \to \bar{Y}_j \qquad Z_j \to \bar{X}_j \tag{D.67}$$

$$Y_j \to -\bar{Z}_j \bar{X}_j \qquad Y_j \to \bar{Y}_j \bar{Z}_j \tag{D.68}$$

D.6 Boundaries

We have already looked at the boundaries of Ashkin-Teller and pCL. The mapping between XXZ and pCL is also of interest.

D.6.1 Periodic Boundaries

We see that the perturbed cluster model on periodic boundaries maps to the periodic XXZ model. Looking at periodic boundaries on XXZ, we see the Hamiltonian is

$$\begin{aligned} H_{XXZ} = &-\beta[\bar{Y}_N\bar{Y}_1 + \bar{X}_N\bar{X}_1 - \lambda\bar{Z}_N\bar{Z}_1] - \sum_{j=1}^{N} \bar{X}_j\bar{X}_j + \bar{Y}_j\bar{Y}_j - \lambda\bar{Z}_j\bar{Z}_j - \\ &\sum_{j=1}^{N-1} \beta\left[\bar{Y}_j\bar{Y}_{j+1} + \bar{X}_j\bar{X}_{j+1} - \lambda\bar{Z}_j\bar{Z}_{j+1}\right]. \end{aligned} \tag{D.69}$$

Mapping this onto AT, for the boundary term, we obtain

$$\bar{Y}_N\bar{Y}_1 \to \sigma_1^X\sigma_N^X S_{AT,1}^N \qquad \bar{X}_N\bar{X}_1 \to \tau_1^X\tau_N^X S_{AT,1}^N \tag{D.70}$$

$$\bar{Z}_N\bar{Z}_1 \to \sigma_1^X\tau_1^X\sigma_N^X\tau_N^X S_{AT,1}^N S_{AT,1}^N. \tag{D.71}$$

where the 'string' operators $S_{AT,1}^N$ and $S_{AT,1}^N$ are σ^Z and τ^Z applied to all sites from 1 to N, the symmetry operators of $\mathbb{Z}_2 \otimes \mathbb{Z}_2$.

D.6.2 Even Chains

The 'natural' boundaries for the cluster model give a pair of qubits encoded on the edge spins. These map into the XXZ and AT as

$$X_1Z_1 \to \bar{X}_1 \to \tau_1^X S_{AT,1}^N \qquad Z_NX_N \to \bar{Y}_N \to S_{AT,1}^N\sigma_N^X \tag{D.72}$$

$$Z_1 \to \bar{Y}_1 \to \sigma_1^X \qquad Z_N \to \bar{X}_N \to \tau_N^X \tag{D.73}$$

D.6.3 Odd Chains

D.6.3.1 Ending in Red

If we consider terminating the chain with a red spin, then we get

$$Z_{N-1}X_{N-1}Z_N \to \bar{Y}_{N-1}\bar{Y}_N \to \sigma_{N-1}^X\sigma_N^X \tag{D.74}$$

$$Z_{N-1}X_N \to \bar{X}_{N-1}\bar{X}_N \to \tau_{N-1}^X\sigma_N^Z \tag{D.75}$$

$$Z_N \to \bar{Y}_N \to \left(\prod_{k=1}^{N-1}\tau_k^Z\right)\sigma_N^X \tag{D.76}$$

D.6.3.2 Starting with Blue

We could consider starting the chain with a blue spin. Then we would obtain

$$Z_1X_2Z_2 \to \bar{X}_1\bar{X}_2 \to \tau_1^X\tau_2^X \tag{D.77}$$

$$X_1Z_2 \to \bar{Y}_1\bar{Y}_2 \to \sigma_2^X \tag{D.78}$$

$$Z_1 \to \bar{X}_1 \to \tau_1^X\left(\prod_{j=2}^{N}\sigma_K^Z\right) \tag{D.79}$$

We have now shown that the map between the XXZ and pCL models is local, and boundary terms remain localised to the boundary under this operation. From this, we conjecture that the CFT describing the thermodynamic limit of the pCL is that describing the XXZ model, namely the S^1 boson.

Appendix E

Compactified Boson Conformal Field Theory

In this appendix, we will describe the spectrum S^1 boson and $S^1/\mathbb{Z}_2$ orbifold boson conformal field theories. These are thought to respectively describe the thermodynamic limit of the perturbed cluster and Ashkin-Teller spin chains. The compactified free boson is a commonly used theory in many fields, and more details can be found in [33–35, 37]. Here, we will simply state the result, emphasising the difference between the two theories. We will use the words fields and states interchangeably, since there is a one to one map between them, with the states being the result of acting with the field operator on the vacuum $|0\rangle$.

E.1 S^1 boson

The S^1 boson CFT is the field theory of a free massless boson on a circle. The field $\varphi(x,t)$ takes an angular value at each point on the circle, and is thus subject to periodic boundary conditions

$$\varphi(x+L,t) = \varphi(x,t) + 2m\pi R, \tag{E.1}$$

where R is the minor radius of the torus traced out by the possible field values and L is the circumference of the circular dimension. We can think of φ as a closed string on the surface of a torus. This gives a convenient interpretation of e, m. m can be seen as the number of times the string wraps around the torus before the ends are joined as in fig. E.0.1. Clearly these are topologically distinct states, so define different sectors. The second quantum number e is a quantised momentum associated with the centre of mass motion.

This defines a set of quasivacuum states $|(e,m);(0,0,\ldots,0),(0,0,\ldots,0)\rangle$ which are all annihilated by all L_n for $n > 0$. The descendant states can then be constructed by acting with creation operators $L_n(\bar{L}_n)$,

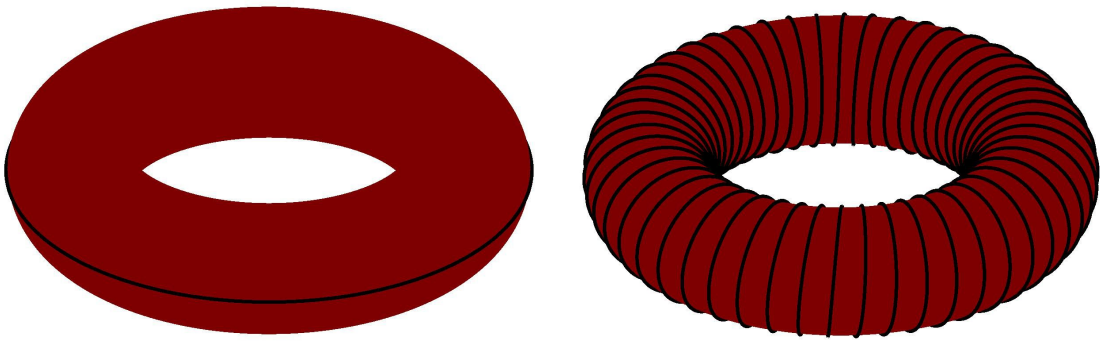

Figure E.0.1 : Quasivacuum states are defined by their winding number m and the centre of mass momentum e.

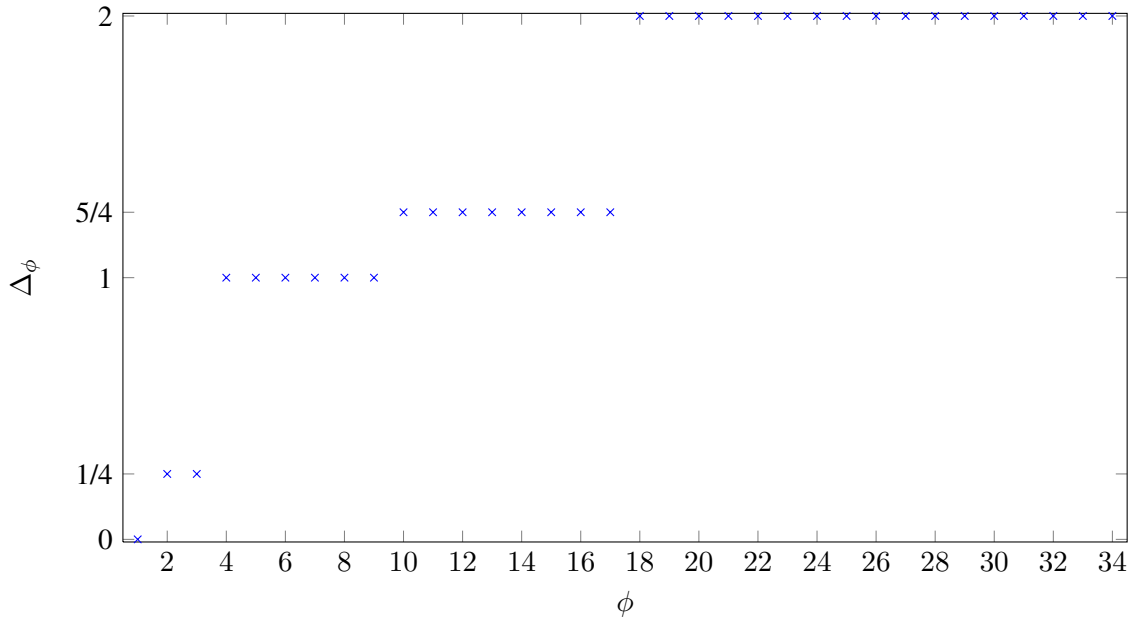

Figure E.1.1 : The full spectrum of the S^1 boson CFT at $R^2 = 1$.

$n < 0$, adding left(right) going waves. These are then states which look

$$L_{-1} \left|(e,m);(0,0,\ldots,0),(0,0,\ldots,0)\right\rangle = \left|(e,m);(1,0,\ldots,0),(0,0,\ldots,0)\right\rangle, \tag{E.2}$$
$$\bar{L}_{-2} \left|(e,m);(0,0,\ldots,0),(0,0,\ldots,0)\right\rangle = \left|(e,m);(0,0,\ldots,0),(0,1,\ldots,0)\right\rangle. \tag{E.3}$$

Notice that adding 2 quanta using L_{-2} does not give the same state as L_{-1}^2.

The scaling dimensions and spin numbers of the vacuum states for this theory are given by [33]

$$\Delta_{e,m} = \frac{e^2}{R^2} + \frac{m^2 R^2}{4}, s = em. \tag{E.4}$$

Under the replacement $R \to 2/R$, we observe a duality between e and m, they simply swap roles. Thus, we can equivalently think of e as a winding number or m as a momentum.

The states

$$L_{-1} \left|(0,0);(0,0,\ldots,0),(0,0,\ldots,0)\right\rangle = \left|(0,0);(1,0,\ldots,0),(0,0,\ldots,0)\right\rangle, \tag{E.5}$$
$$\bar{L}_{-1} \left|(0,0);(0,0,\ldots,0),(0,0,\ldots,0)\right\rangle = \left|(0,0);(0,0,\ldots,0),(1,0,\ldots,0)\right\rangle, \tag{E.6}$$
$$L_{-1}\bar{L}_{-1} \left|(0,0);(0,0,\ldots,0),(0,0,\ldots,0)\right\rangle = \left|(0,0);(1,0,\ldots,0),(1,0,\ldots,0)\right\rangle, \tag{E.7}$$

turn out to act as primary fields in this theory, with eqn. E.7 being the marginal field.

Recall that the radius of this theory is related to the parameter in the perturbed cluster model via

$$R^2 = \frac{2}{\pi}(\pi - \cos^{-1}\lambda). \tag{E.8}$$

The relevant spectrum at the point $\lambda = 0, R = 1$ is shown in fig. E.1.1 By varying the radius of the compactification, we vary the scaling dimensions as shown in fig. E.2.2 (a).

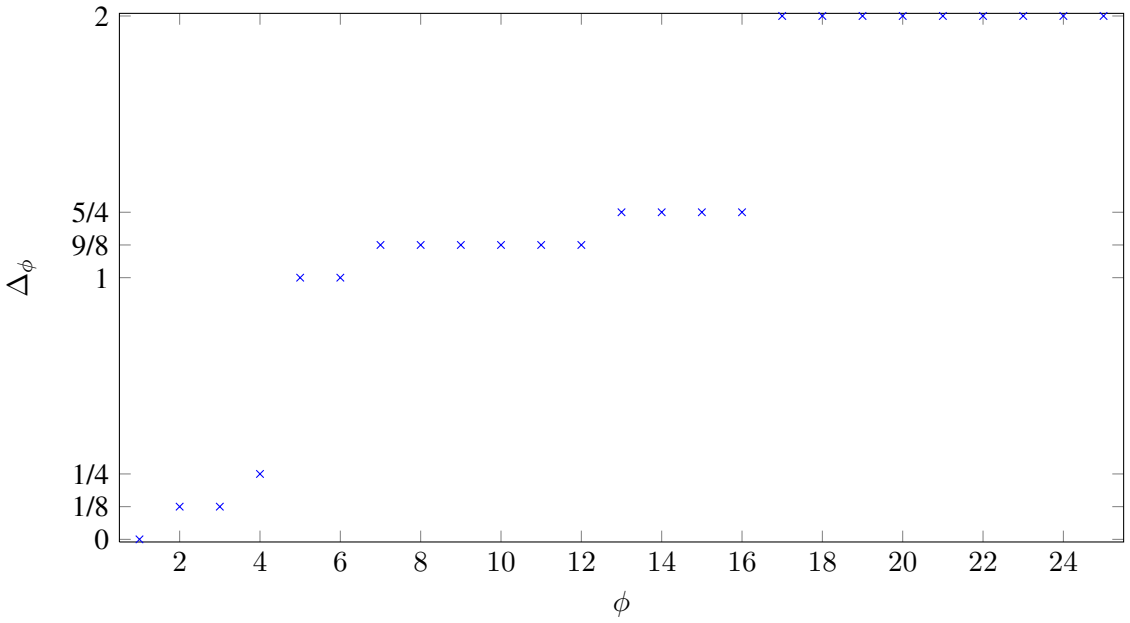

Figure E.2.1 : The full spectrum of the $S^1/\mathbb{Z}_2$ orbifold boson CFT at $R^2 = 1$.

E.2 $S^1/\mathbb{Z}_2$ orbifold boson

The orbifolded theory is constructed by identifying $\varphi \equiv -\varphi$ [37]. The result is that states must transform to themselves under the swap $e \leftrightarrow -e$, $m \leftrightarrow -m$; they must be positive parity states. As such, we redefine our vacuum states by taking advantage of the degeneracy of $|e, m\rangle$ and $|-e, -m\rangle$. Our new vacuum states are

$$|(e,m)\rangle_+ = |(e,m)\rangle + |(-e,-m)\rangle\,, \tag{E.9}$$
$$|(e,m)\rangle_- = |(e,m)\rangle - |(-e,-m)\rangle\,, \tag{E.10}$$

where the lack of photons is left implicit. The $|\rangle_+$ states are clearly allowed in the orbifold theory, however the $|\rangle_-$ states are now forbidden and do not occur. As such, we get a halving in the degeneracy.

Adding a single photon to any of the oscillator modes is negative parity, so adding single photons to $|\rangle_+$ states gives forbidden descendants, whereas $|\rangle_-$ with odd numbers of photons are now allowed descendants. So on for adding even photon numbers. Recall that L_{-2} adds a single photon worth 2 quanta.

The orbifold theory also permits a set of 'twist' fields associated with the twisted boundary conditions $\varphi(x+L) = -\varphi(x)$. These have fixed scaling dimensions of $1/8$, and are doubly degenerate. The photons in the twisted sector are still negative parity, but only add $1/2$ to the scaling dimension rather than 1. We now call these operators $L_{-1/2}$, $L_{-3/2}$ and so on.

The radius is related to the Ashkin-Teller coupling parameter via

$$R^2 = \frac{\pi}{2}\frac{1}{\cos^{-1}(-\lambda)}. \tag{E.11}$$

This then has the nice property that $R = 1$ when $\lambda = 0$. The spectrum at this point is shown in fig. E.2.1. Once again, we can vary the scaling dimensions by varying the radius, as shown in fig. E.2.2 (b).

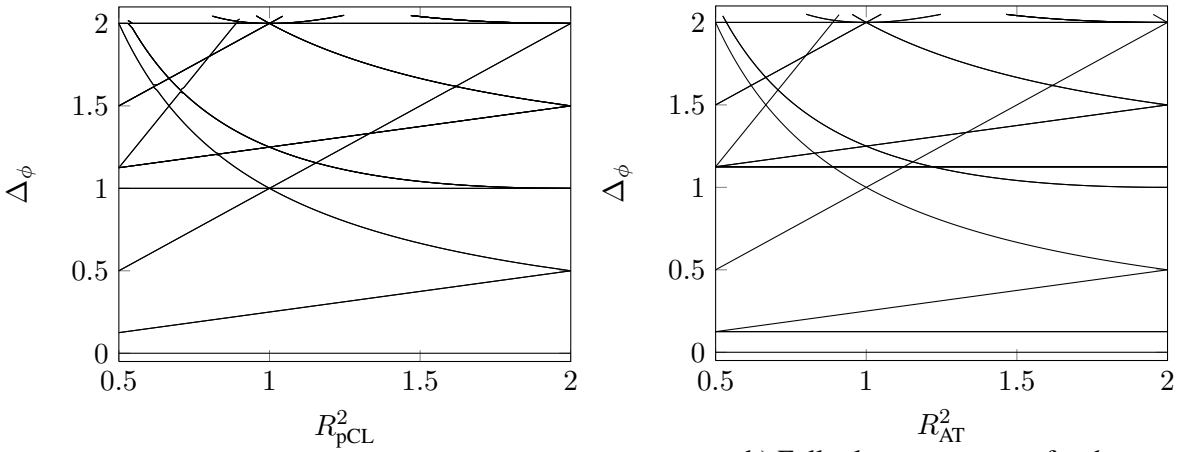

a) Full relevant spectrum for the S^1 boson CFT.

b) Full relevant spectrum for the $S^1/\mathbb{Z}_2$ orbifold boson CFT.

Figure E.2.2 : Full spectra for the two CFTs as the radii are varied. Notice the presence of the twist fields at constant scaling dimensions $1/8$, $9/8$ and the absence of the fields with dimension 1 in (b).